

## Shear wave attenuation and dispersion in melt-bearing olivine polycrystals:

### 2. Microstructural interpretation and seismological implications

Ulrich H. Faul, John D. Fitz Gerald, and Ian Jackson

Research School of Earth Sciences, The Australian National University, Canberra, Australia

Received 16 January 2003; revised 22 December 2003; accepted 31 March 2004; published 23 June 2004.

[1] The torsional forced oscillation tests of melt-bearing olivine aggregates reported by Jackson *et al.* [2004] consistently show a peak in attenuation that is absent from melt-free aggregates tested under similar conditions and grain sizes. Characterization by SEM shows that the melt resides in triple junction tubules and larger pockets as previously described. TEM imaging and EDS analysis reveals that olivine-olivine grain boundaries are characterized by a region  $\leq 1$  nm wide which is structurally and chemically distinct from olivine grain interiors. From the possible mechanisms that can produce an anelastic attenuation peak, melt squirt can be eliminated for our samples and experimental conditions. We attribute the observed attenuation peak to elastically accommodated grain boundary sliding, requiring that the grain boundaries are weak relative to olivine grain interiors but have a significantly higher viscosity than bulk melt. While the nanometer scale grain boundary structure in the melt-bearing aggregates is essentially the same as for melt-free aggregates studied previously, elastically accommodated sliding in the latter is apparently inhibited by tight three-grain edge intersections. The exponentially increasing high temperature background attenuation in both types of aggregate is attributed to diffusionally accommodated grain boundary sliding. Extrapolation to mantle grain sizes shows that the broad peak may be responsible for nearly frequency independent attenuation in partially molten regions of the upper mantle. **INDEX TERMS:** 5102 Physical Properties of Rocks: Acoustic properties; 5112 Physical Properties of Rocks: Microstructure; 5144 Physical Properties of Rocks: Wave attenuation; 3909 Mineral Physics: Elasticity and anelasticity; **KEYWORDS:** seismic wave attenuation, olivine, partial melting, grain boundary sliding, grain boundary structure, attenuation peak

**Citation:** Faul, U. H., J. D. Fitz Gerald, and I. Jackson (2004), Shear wave attenuation and dispersion in melt-bearing olivine polycrystals: 2. Microstructural interpretation and seismological implications, *J. Geophys. Res.*, 109, B06202, doi:10.1029/2003JB002407.

#### 1. Introduction

[2] In order to investigate the effect of the presence of melt on shear modulus and attenuation in rocks representative of the upper mantle, we conducted torsional forced oscillation and microcreep experiments on melt-bearing olivine polycrystals as described in detail by Jackson *et al.* [2004]. All six specimens show a broad peak in attenuation, superimposed on a dissipation background enhanced relative to that for melt-free aggregates [Jackson *et al.*, 2004]. For each specimen the peak is of fixed height and shape, while the dissipation background increases monotonically with increasing oscillation period and temperature. Amongst the specimens a positive correlation is apparent both for peak height with melt fraction [Jackson *et al.*, 2004, Figure 10] and peak width with the width of the grain-size distribution. In plots of dissipation vs. period the peak moves in a relatively narrow temperature interval

(1000°C to 1300°C) across the observational window (1 to 1000 s), reflecting a very high activation energy  $E_p$ . As for the melt-free samples, the background dissipation of the melt-bearing samples decreases with increasing grain size and increases with increasing period. At 1000°C the melt-bearing samples have essentially the same background dissipation levels as the melt-free samples, but the dissipation levels diverge increasingly with increasing temperature, requiring a higher background activation energy  $E_B$  for the melt-bearing samples. In the following, sample chemistry and melt distribution are discussed first, then models are examined which could explain the observations. Finally the experimental results are extrapolated to mantle conditions.

#### 2. Sample Characterization

##### 2.1. Overview

[3] Sample characterization after mechanical testing included light microscopy, SEM imaging, EDS and

**Table 1.** Sample Characteristics

Sample	Origin	Starting Grain Size, $\mu\text{m}^a$	Grainsize $\mu\text{m}^b$	Glass Added, wt%	Melt Content <sup>c</sup> , vol.%	Time at Max. Temperature <sup>d</sup>	[H <sub>2</sub> O], wt. ppm <sup>e</sup>
AT6380	San Carlos	2–10	6.5	-	0.01	44h, 1200°C	<10
AT6335	San Carlos	2–10	8.9	3.0	2.1	6h, 1280°C	10
AT6410	Sol-Gel	<1	11.3	2.0	1.5	15h, 1300°C	20
AT6384	Sol-Gel	<1	27.5	4.0	3.7	42h, 1300°C	70
AT6409	San Carlos	10–38	29.3	2.0	1.3	30h, 1300°C	20
AT6366	San Carlos	2–10	52.3	-	0.4	110h, 1240°C	80

<sup>a</sup>Grainsize prior to hot pressing from settling in ethanol (San Carlos derived) or after reacting of the gel in the controlled oxygen atmosphere furnace (Sol-Gel, see *Jackson et al.* [2002] for more details).

<sup>b</sup>Mean grain size after testing obtained from EBSD mapping, multiplied by  $4/\pi$  to correct for sectioning effects.

<sup>c</sup>Melt content at maximum temperature determined by image analysis.

<sup>d</sup>Time includes both hot-pressing and testing at that temperature.

<sup>e</sup>The column indicates the bulk water content determined by FTIR.

WDS analysis, electron backscatter diffraction mapping to determine grain size distributions, and TEM analysis and imaging of selected samples. The water content was determined by Fourier transform infrared analysis. None of the samples show evidence for H<sub>2</sub>O structurally bound in olivine in their infrared spectra. Instead the small amounts of water ( $\leq 80$  ppm) must reside in the glass or pores. All samples are within 1% of theoretical density, as determined by immersion in ethanol. Table 1 summarizes the sample properties including average grain size and melt content.

[4] To produce a basaltic melt at run conditions, oxide-derived glass was added to the olivine powders by grinding

both together in an agate mortar. The composition of the added glass is given in Table 2. The melt in AT6366 and AT6380 is associated with impurities in the San Carlos olivine starting material. Samples derived from sol-gel precursors [see *Jackson et al.*, 2002] were designed to contain a limited excess of SiO<sub>2</sub> relative to olivine stoichiometry, resulting in the crystallization of a small volume fraction of orthopyroxene (opx). Except for small amounts of opx crystallized from the melt during staged cooling, the samples made from San Carlos olivine contain no opx.

[5] Pores with diameters ranging from a few microns to submicron occur throughout grains of all samples. Coarser-grained samples (AT6409 and AT6366, Figures 1c

**Table 2.** Phase Compositions of AT6384 and Reequilibrated Samples<sup>a</sup>

Temperature	MgO	Al <sub>2</sub> O <sub>3</sub>	SiO <sub>2</sub>	CaO	TiO <sub>2</sub>	FeO	Na <sub>2</sub> O	K <sub>2</sub> O	Phase Prop., vol% <sup>b</sup>
	<i>Melt/Glass</i>								
Starting glass	11.6	13.9	47.9	10.7	2.4	10.7	2.2	0.5	
1300°C	5.4	14.9	58.7	9.7	2.5	5.6	2.8	0.4	3.7
Melt (calc.) <sup>c</sup>	10.5	12.0	49.2	7.4	2.5	15.2	2.5	0.6	
1250°C	3.8	16.6	57.6	10.5	2.8	5.2	3.0	0.5	
1200°C	3.6	17.8	57.7	10.4	2.7	4.2	3.2	0.5	2.9
1150°C	2.6	17.3	58.4	10.0	3.3	4.1	3.5	0.7	
Staged cool <sup>d</sup>	2.6	20.5	63.0	6.3	1.5	1.6	3.6	0.8	
	<i>Clinopyroxene</i>								
Staged cool	15.4	11.2	45.3	19.2	4.5	4.0	0.4		
	<i>Plagioclase<sup>e</sup></i>								
1150°C	4.2	25.8	52.6	11.9	0.2	1.3	4.0	0.1	
	<i>Orthopyroxene</i>								
1300°C	34.0	1.2	56.6	1.1	0.3	6.8			0.9
1250°C	34.0	1.2	56.9	1.0	0.0	6.8			
1200°C	34.1	0.7	57.3	0.8	0.3	6.7			4.0
1150°C	33.5	1.1	56.8	1.3	0.4	6.7			
Staged cool	33.9	1.1	56.5	1.2	0.3	6.9			
	<i>Glass Composition of Other Samples</i>								
AT6410	5.4	19.6	60.8	5.9	1.4	2.0	4.1	0.8	
AT6409	1.3	26.3	55.5	10.8	0.4	0.7	4.8	0.3	
AT6335	6.7	18.4	60.7	8.1	1.1	2.0	2.9	0.2	
AT6366 <sup>f</sup>	12.9	11.9	67.7	0.5	0.0	2.3	2.8	2.0	

<sup>a</sup>Compositions determined by standardized EDS analysis are given in wt%. Glass compositions are indicative only due to modification during cooling/quench, and beam overlap with adjacent crystals for small melt pockets.

<sup>b</sup>Phase proportions determined by processing BSE images.

<sup>c</sup>Melt composition calculated by mass balance.

<sup>d</sup>This is the composition of a mix of mostly nanotwinned plagioclase with some interstitial glass (c.f. Figure 5).

<sup>e</sup>After re-equilibration at 1150°C, glass and plagioclase are distinctly different at the  $\mu\text{m}$  scale, the plagioclase composition is near stoichiometric.

<sup>f</sup>A Cl peak was also present in the EDS spectra.

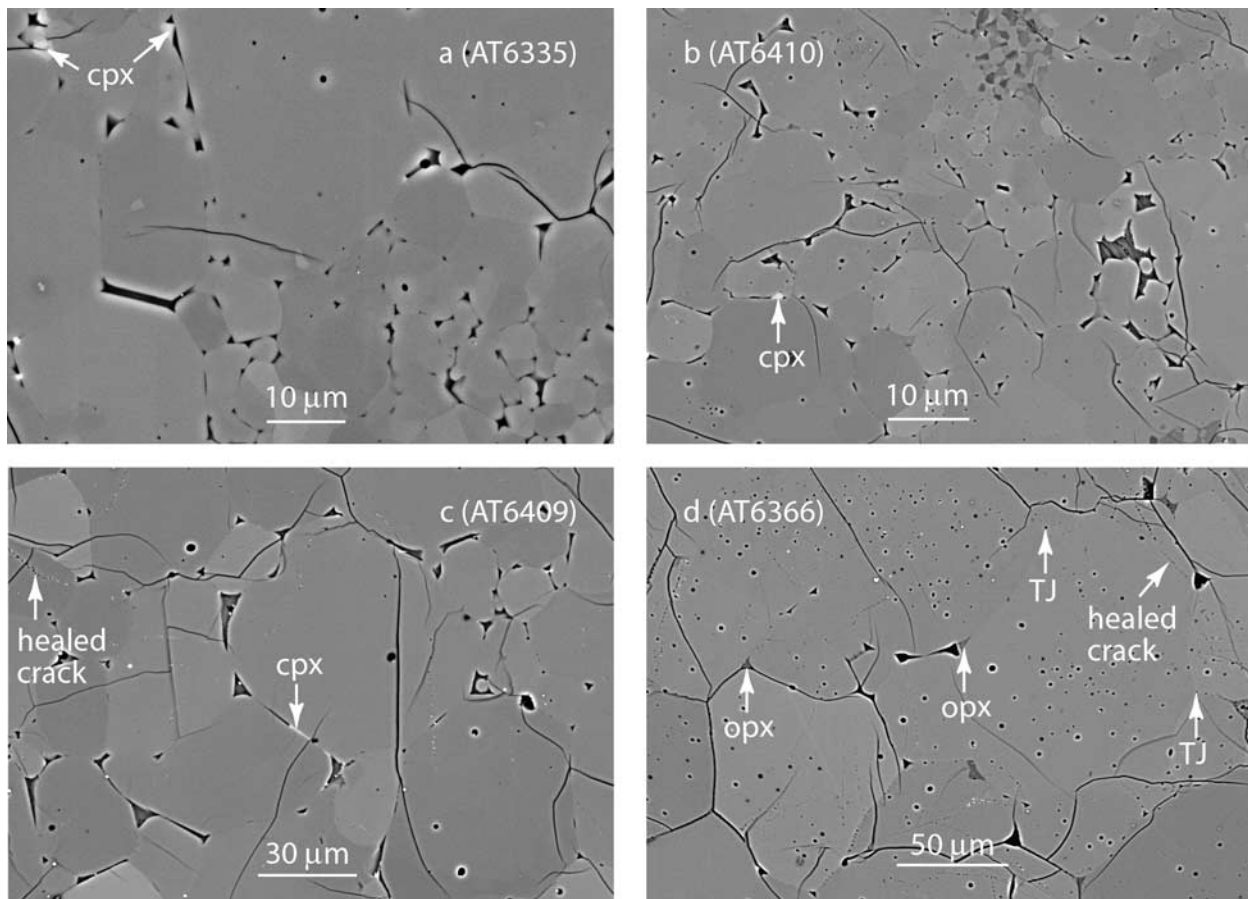


**Figure 1.** Backscattered electron images of four samples tested in this study. The images have a relatively high contrast setting so that individual grains are visible. The high contrast setting causes the melt to be very dark, and exaggerates somewhat the size of cracks and pores. (a) The image of sample AT6335 illustrates the broad range in grain size due to the relatively short anneal time at the highest temperature relative to the other samples. The melt inclusions in areas with small grains also tend to be smaller than those adjacent to large grains. Minor amounts of cpx are indicated by arrows. (b) Sample AT6410 has a similar mean grain size as AT6335 but a narrower grain size distribution. The arrow points to a cpx grain. Near the top is a cluster of intergrown opx and olivine grains residual from the sol-gel synthesis. Some opx crystallized during staged cooling as in AT6384. (c) Sample AT6409 has a similar mean grain size to AT6384 but the melt content is less than half that of AT6384. Minor amounts of cpx in some cases crystallized on two-grain boundaries (arrow), but no opx was found. (d) Sample AT6366 with one of the lowest melt contents of the six samples. The arrows point to interstitial opx (dark patches, center of the image) or three-grain edges (TJ) where no melt can be resolved by SEM. The total melt content in this image (opx + near black glass at three-grain edges) is higher than average; some areas of similar or larger size contain very little SEM-resolvable melt.

and 1d) contain pores in planar arrays, indicating healing of cracks which resulted from previous thermal cycling (note that the modulus and dissipation data presented by Jackson *et al.* [2004] were obtained during staged cooling after several hours of annealing at the highest temperature). For AT6384, the glass in each of a small number of triple junctions also contains a single large pore. Cracks in the recovered specimens increase in size and number with increasing grain size, confirming previous indications that the threshold for pervasive thermal microcracking is  $\sim 30 \mu\text{m}$  [e.g., Tan *et al.*, 2001]. Except for AT6366 with a low melt fraction and large grain size these cracks generally do not follow grain boundaries but are apparently randomly distributed and oriented. Minor

graphite and metallic blebs, both arising from aggregate production, are present inside olivine or at grain boundaries.

## 2.2. Melt Distribution

[6] The microstructures of the samples are dominated by olivine grains with convex grain boundaries relative to the melt and overall intergranular melt geometries characteristic of grain growth in the absence of deformation. The melt is evenly distributed at the sample scale; no gradients in melt fraction either radially or longitudinally were found. The melt distribution is similar to that described previously [e.g., Waff and Bulau, 1979; Faul *et al.*, 1994; Hirth and Kohlstedt, 1995]. All

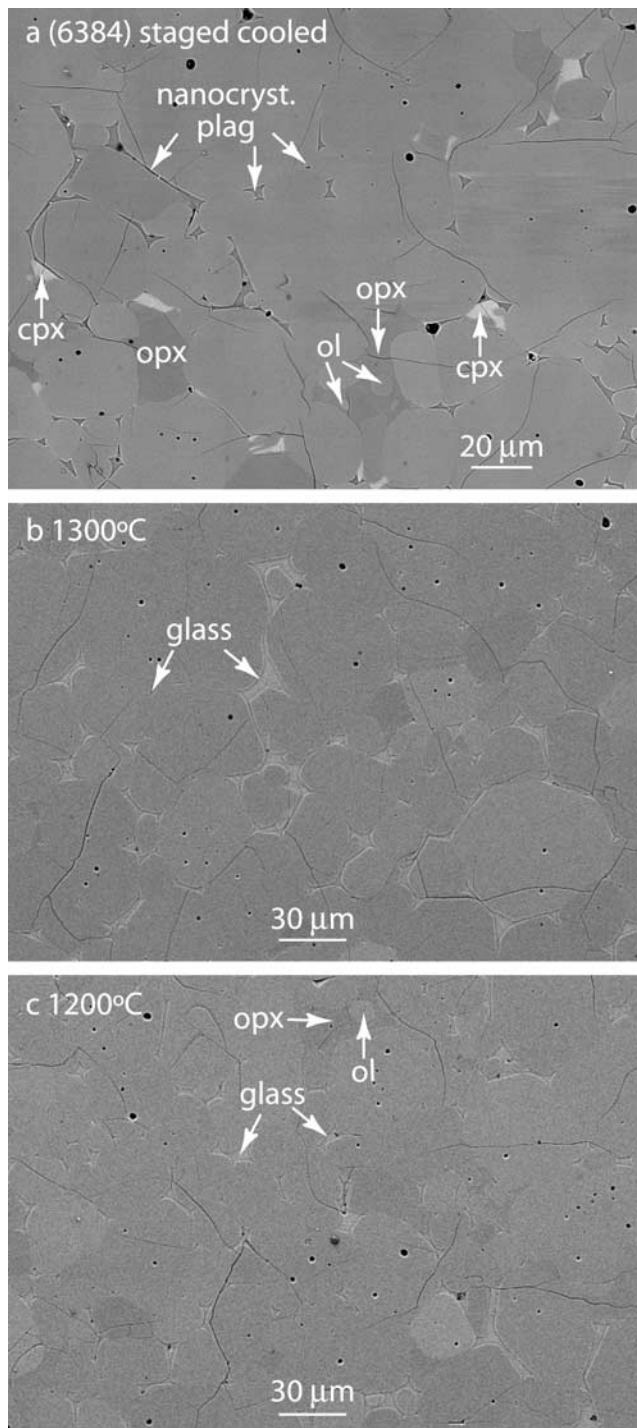


**Figure 2.** (a) Backscattered electron (BSE) image of sample AT6384. Olivine grains are light grey, opx darker, cpx almost white. The former melt is darkest, its composition approaches that of plagioclase. (b) A slice of AT6384 re-equilibrated at 1300°C for six hours and quenched. Only a few opx grains are present but no cpx. The melt content determined from images relative to the amount of glass added indicates only a small amount of olivine crystallization. (c) A slice of AT6384 re-equilibrated at 1200°C. More opx crystallized while some olivine dissolved (Table 2). The character of the melt distribution is essentially unchanged relative to the sample quenched from 1300°C.

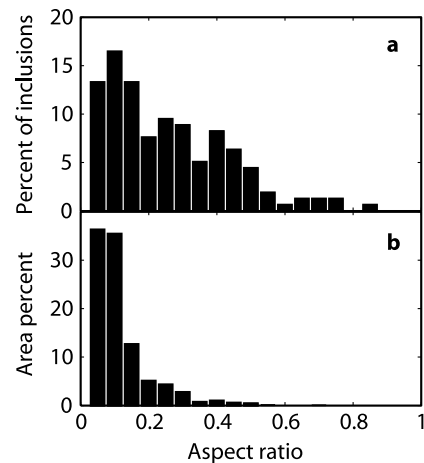


**Figure 3.** Aspect ratio distribution of melt inclusions, determined from BSE images from a slice of AT6384 re-equilibrated and quenched from 1300°C. The method is described by *Faul et al.* [1994]. (a) Distribution as a function of the total number of inclusions. (b) Distribution as a function of the area of inclusions sorted by aspect ratio. The distributions are similar to those reported by *Faul et al.* [1994], with most of the melt by volume in low aspect ratio inclusions.

three-grain edge intersections contain melt, however the size and shape of the triple junction tubules varies greatly (Figures 1 and 2). Larger, more irregular-shaped melt inclusions are also evident, especially at higher melt fraction. Both rounded and flat crystal melt interfaces occur. Aspect ratios of melt inclusions as shown in Figures 1 and 2 have been determined in a detailed analysis of partially molten olivine aggregates with very similar melt composition, melt content and grain size by *Faul et al.* [1994]. Figure 3 shows the aspect ratio distribution from a slice of AT6384 re-equilibrated at 1300°C (see section 2.4 below), following the method described by *Faul et al.* [1994]. The distribution is very similar to those described earlier; the minimum aspect ratio is 0.025. No differences in melt geometry are observable in the other samples that would suggest substantially lower aspect ratios.

### 2.3. Grain-Size Distributions

[7] The grain-scale melt distribution (Figures 1 and 2) is influenced by the grain size distribution (Figure 4); the narrower the grain size distribution the more uniform the melt distribution appears. The normalized grain-size distributions show that AT6335 has the broadest and AT6384 the narrowest distribution, the latter indicative of steady state grain growth. The shape of the grain-size distribution is independent of the sample origin as sol-gel or San Carlos olivine. The broad grain size distribution of AT6335 and AT6380 [*Jackson et al.*, 2002], indicative of an immature texture, is the result of the much shorter duration and lower temperature of hot pressing and annealing prior to testing (Table 1). For AT6410 the time spent at 1300°C was minimized to limit grain growth, this also resulted in a broader grain-size distribution relative to AT6384. AT6409 started from larger grain sizes, which

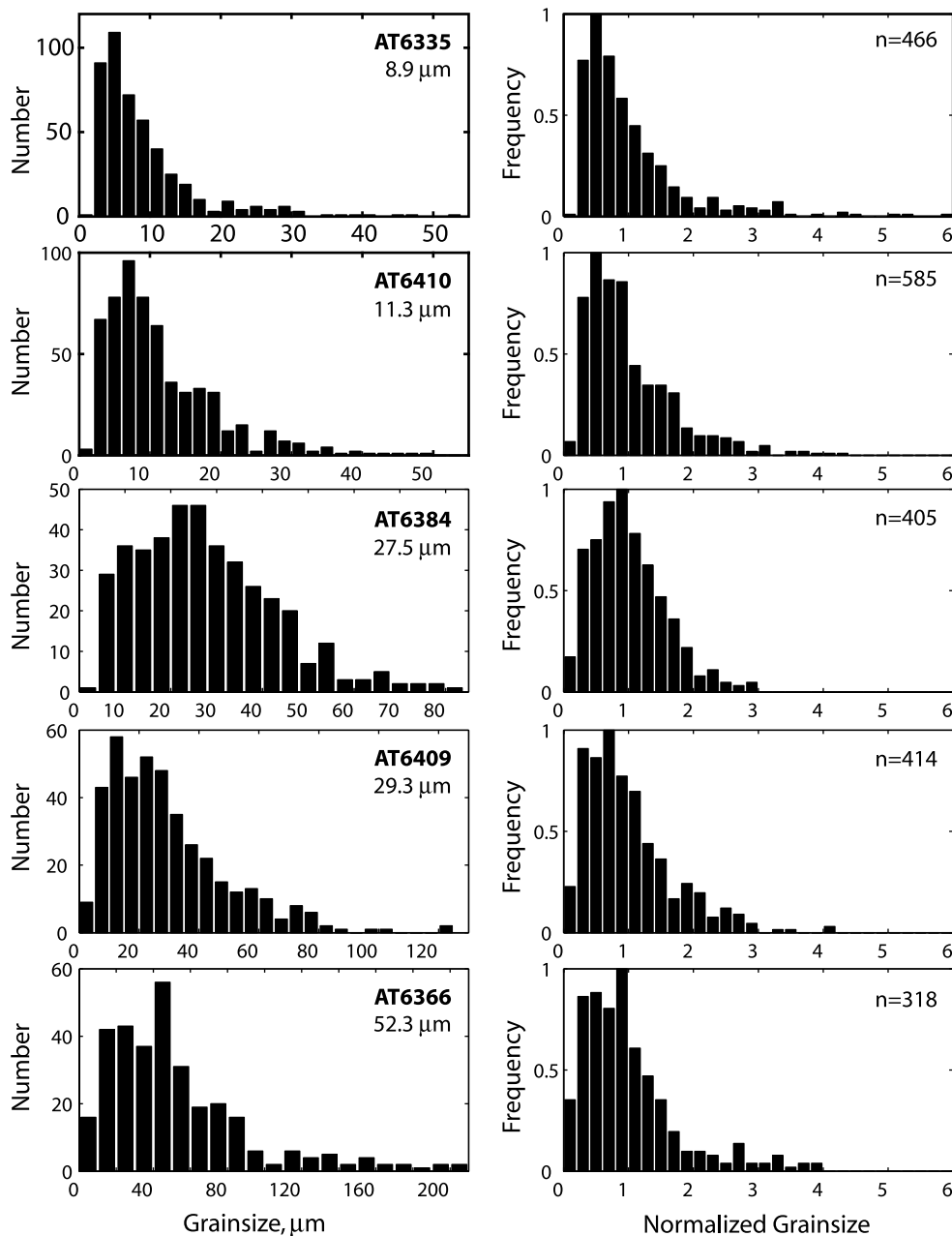


**Figure 4.** Grain size distributions determined by EBSD. The mean grain size for each sample is indicated on the panels in the left column. The normalized grain size distributions in the right column show more clearly the differences between the samples, the numbers indicate the number of grains measured. AT6335 has the broadest distribution corresponding to the shortest anneal time at peak temperature (Table 1). AT6384 has the narrowest distribution with the longest time at peak temperature and a small starting grain size. The grain-size distribution for AT6380 is given by *Jackson et al.* [2002, Figure 2] and is most comparable to that of AT6335.

evolve more slowly toward a steady state distribution. Amongst the six specimens the mean grain size ranges from 6.5 to 52  $\mu\text{m}$  (Table 1). Comparison of the starting grain size with the grain size after testing shows that all samples experienced significant grain growth. The most rapid grain growth occurred during hot pressing; for example the mean grain size of specimen 6384 after hot pressing for 24 hours at 1300°C is 20.0  $\mu\text{m}$ , on further annealing for 18 hours prior to mechanical testing during

staged cooling the final grain size of 27.5  $\mu\text{m}$  was established.

#### 2.4. Microstructures and Crystallization During Staged Cooling

[8] In order to characterize the textures, progressive crystallization and melt contents during mechanical testing (during staged cooling in 50° intervals to room temperature from the maximum temperature), slices cut from AT6384

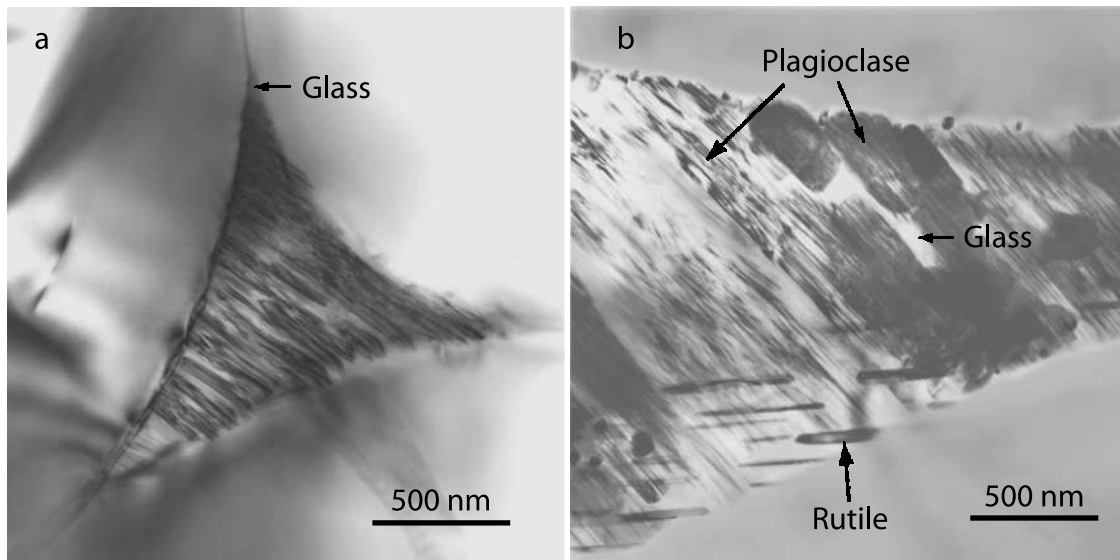


**Figure 5.** TEM images of nanocrystalline plagioclase from sample AT6384 after staged cooling. (a) The region shaped like a triple junction tubule once filled with basaltic melt has almost completely crystallized into one crystal of plagioclase. Narrow twins running right across the plagioclase crystal indicate its crystallographic continuity. Small amounts of residual glass are trapped where the crystal changes its orientation abruptly. The arrowed tip of the triple junction also contains residual glass. (b) Part of a larger melt pocket containing nanocrystalline plagioclase, residual glass and minor rutile after staged cooling. All of the melt pockets and triple junctions in Figure 2a contain this nanotwinned plagioclase with a small amount of residual glass in the staged cooled sample.

were reequilibrated at 50°C intervals from 1300°C to 1150°C. The slices were returned to the target temperature in the same sample assembly as for hot pressing and testing, reequilibrated for 6 h (24 h for the 1150°C sample) and quenched.

[9] Examples from specimens reequilibrated at 1300°C and 1200°C, respectively, are shown in Figure 2 and Table 2. At 1300°C little orthopyroxene (opx) is present (Figure 2b), and no olivine grains are found inside opx. At 1200°C more opx has crystallized (Figure 2c) with a few small olivine grains now inside large opx patches, and a somewhat lower residual melt content (Table 2). This indicates that opx crystallization is accompanied by olivine dissolution. Crystallizing opx in some cases also completely displaced the melt from three-grain edge intersections. Careful TEM examination of glass in the 1300°C slice reveals no evidence for the presence of quench crystals although epitaxial growth of olivine and/or opx cannot be ruled out.

[10] The clinopyroxene (cpx) evident in the staged cooled sample (Figure 2a) commonly shares a sharp planar (100) interface with an adjacent opx crystal and is aligned such that crystallographic directions, e.g., [010], are parallel. This indicates that the cpx grew epitaxially on earlier grown opx.

[11] TEM observations on the staged-cooled samples show that plagioclase (plag) crystallizes extensively throughout the melt pockets and triple junctions at a temperature not far from 1150°C (as indicated by the sample reequilibrated at that temperature). This plagioclase has a complex microstructure with many narrow twins (presumably produced from symmetry change during cooling) commonly revealing that only one crystal orientation grew across the previously liquid region (Figure 5),

leaving almost no glass residue. In detail however, each plagioclase is a mosaic of nearly aligned, submicron domains, and very small volumes of residual glass occur throughout the twinned plagioclase at domain boundaries. Residual glass, usually in slightly larger abundance, is also present at plag-plag grain boundaries where the crystal orientation changes abruptly. Overall, the residual glass fraction in the plagioclase regions in the staged cooled sample AT6384 is only 1–2 vol%. Nanocrystals of rutile commonly line the olivine-plagioclase interfaces, balancing the low TiO<sub>2</sub> content of the melt/plagioclase of the staged cooled sample.

[12] In summary, during cooling from the maximum test temperature of 1300°C to 1200°C only opx crystallizes; the character of the melt distribution is largely unchanged. The most significant changes in melt content and composition develop over a relatively narrow temperature interval between about 1200°C and 1150°C where cpx and plagioclase crystallize. Below 1150°C the residual melt/glass content is smaller than 0.05% of the sample, i.e., the sample is 99.95% crystalline.

[13] Sample AT6384 with the largest amount of added basaltic glass and therefore the highest melt content at the maximum test temperature shows the greatest extent of crystallization of opx and cpx. The other samples (except AT6366 and AT6380) that had a smaller amount of added basaltic glass similarly crystallized cpx (indicated by arrows in Figures 1a–1c) and opx, but only in minor amounts. The effective melt content in the melt added samples AT6335, AT6410 and AT6409 (i.e., either melt or nanocrystalline plagioclase with residual glass), as well AT6380 is therefore within error the same over the whole temperature range for mechanical testing. Only AT6384 and possibly AT6366

**Table 3.** Olivine Compositions From Microprobe WDS Analyses<sup>a</sup>

Sample and Origin	SiO <sub>2</sub> , wt %	MgO, wt %	FeO, wt %	Al <sub>2</sub> O <sub>3</sub> , wt ppm	CaO, wt ppm	TiO <sub>2</sub> , wt ppm	MnO, wt ppm	NiO, wt ppm	Cr <sub>2</sub> O <sub>3</sub> , wt ppm
<i>Melt Present</i>									
AT6366 (SC, 5)	41.2	49.4	8.9	<520 (1)	710	0	1490	2630	470
AT6384 (SG, 5)	41.0	49.0	9.9	<440 (1)	1620	240	<140 (2)	<130 (3)	<320 (4)
AT6410 (SG, 5)	41.1	49.1	9.6	<1090 (4)	1340	<280 (4)	<140 (1)	<130 (1)	<220 (1)
AT6335 (SC, 5)	41.2	49.6	8.5	<546 (4)	1690	<150 (4)	1660	3000	450
<i>Melt Free</i>									
AT6381 (SG, 3)	40.7	49.1	10.2	<650 (1)	<100 (2)	0	0	0	0
AT6261 (SC, 6)	40.2	50.1	9.1	0	920	0	1560	2670	380

<sup>a</sup>SC and SG indicate San Carlos or Sol-Gel origin respectively. The number in parentheses in this column gives the number of analyses averaged. The number in parentheses in the other columns shows how many analyses gave a result above the detection limit. Zero indicates that all analyses were below the detection limit (~420 wt. ppm and ~640 wt. ppm for Al for the slightly different analytical conditions for melt-bearing and melt-free samples respectively).

have a somewhat higher melt content at the maximum test temperatures (Tables 1 and 2).

### 2.5. Sample Chemistry and TEM-Scale Observations of Three-Grain Edges

[14] The compositions of residual glass, opx, cpx and plagioclase (where present) were determined by standardized EDS analysis (Table 2), and the composition of olivine by WDS analysis to quantify its trace element content (Table 3). The phase proportions of melt (glass) and opx were derived from processing backscattered electron (BSE) images, and used to calculate a melt composition by mass balance for the slice of AT6384 reequilibrated and quenched from 1300°C. While the melt compositions are quenched modified and must be viewed with some caution (particularly for AT6366), the systematic increase in incompatible elements (Ti, Na and K) in the melt of the slices of AT6384 quenched from progressively lower temperatures is consistent with a somewhat decreasing melt content due to crystallization.

[15] AT6366 and AT6380 contain only impurity-derived melt and at least AT6366 has a somewhat different melt composition compared to the other samples. For AT6366, because of the small amount of melt and its proportionally more extensive crystallization to opx it was difficult to determine melt content and chemistry accurately. The shape and interstitial nature of most of the opx grains suggests that they crystallized during staged cooling. They were therefore counted as melt in arriving at the 0.4% figure in Table 1. The bulk of the melt resides in a few large triple junctions and more irregular inclusions at three- and four-grain corners. Some three-grain edge intersections appear melt-free at the SEM scale (Figure 1d), but TEM examination of 40 three-grain edge intersections in this specimen showed that every one contains melt.

[16] The glass in AT6366 contains very little CaO, relatively high K<sub>2</sub>O and traces of Cl (Tables 2 and 4). Opx was the main phase to crystallize during staged cooling of this sample; only one small crystal of cpx was found. The presence of other small crystals like phlogopite and magnesite (detected by TEM) further highlights the difference in crystallization behavior compared to AT6384 for example. Melt that is CaO-poor but with significant K<sub>2</sub>O and Cl could originate from glass films on grain boundaries [Wirth, 1996] of the original San Carlos olivine. However, the melt content is relatively high (up to 0.4% if opx is completely

converted to melt at the highest test temperature for this sample), compared with ≤0.01% in specimens made from all other batches of San Carlos olivine [Tan *et al.*, 2001; Jackson *et al.*, 2002].

[17] The average residual glass compositions in the staged-cooled samples AT6366 and AT6384 (i.e., the 0.05% glass interstitial to the plagioclase) are very similar, although there is considerable variability (Table 4). This is quite different to the situation at high temperature where melt compositions were distinctly different and AT6384 contained much more melt.

[18] No melt is detectable in AT6380 by light microscope or SEM. TEM examination of 40 triple junctions shows that 39 contain melt, with a triple-junction tubule diameter around 40 nm. From this a melt content of approximately 0.01% was calculated. No larger, or irregular melt pockets were found. A trace amount of opx is present, primarily at two-grain boundaries. The small size of the glass pockets at three-grain edge intersections precludes quantitative TEM-EDS analyses of the glass; the EDS spectra indicate a relatively high silica content.

[19] Table 3 shows the olivine compositions of four of the melt-bearing samples from this study and two melt-free (meaning in case of the San Carlos derived AT6261 a melt content <0.01%; no glass is detectable by TEM in sol-gel derived samples without added melt) samples from Jackson *et al.* [2002]. Of particular interest is a comparison of the trace element contents of olivine of sol-gel and San Carlos

**Table 4.** Residual Glass Compositions Determined by Analytical TEM (wt% oxide or wt% Cl)<sup>a</sup>

	AT6366 (15 analyses)		AT6384 (7 analyses)	
	Average	Range	Average	Range
MgO	2.4	0.7–5.1	1.8	0.9–2.6
Al <sub>2</sub> O <sub>3</sub>	14.3	1.7–19.7	11.1	7.4–19.6
SiO <sub>2</sub>	76.9	67.5–96.6	77.4	63.1–84.6
CaO	0.2	0–0.9	4.0	1.0–9.6
TiO <sub>2</sub>	0.3	0–0.7	1.2	0.4–1.9
FeO	1.2	0.4–3.4	0.9	0.6–1.3
Na <sub>2</sub> O	2.8	0–7.9	1.7	0.8–3.0
K <sub>2</sub> O	1.5	0–4.0	2.0	0.3–4.9
Cl	0.4			

<sup>a</sup>Ranges indicate considerable compositional variation. Analyses using defocused electron beam around 50–100 nm diameter, normally positioned as far as possible from adjacent crystalline phases. Analytical totals normalized to 100%.

origin. For olivine from melt-free sol-gel samples the trace element content is at or below the detection limit for microprobe WDS analysis, while olivine from the melt-free San Carlos samples contains the expected trace element inventory. In contrast, olivine in the melt-added samples contains essentially the same amount of Ca regardless of its origin (except for AT6366 with very little Ca in the melt). Some Ti was also incorporated into olivine, whereas Mn and Ni, absent from the added melt, are found only in San Carlos origin olivine. Ni loss from San Carlos olivine, typically observed with pure Fe jackets, was suppressed by the use of  $\text{Fe}_{30}\text{Ni}_{70}$  liners surrounding samples (other than 6335) during hot pressing and testing.

### 3. Grain Boundary Structure and Chemistry

#### 3.1. General Features

[20] Olivine grain boundaries (GBs) of samples AT6366, AT6384, and to a lesser extent AT6335 and the slice of AT6384 re-equilibrated at  $1300^{\circ}\text{C}$ , were examined by TEM. Many of the nanoscale features of the GBs are very like those we have previously described [Cmiral *et al.*, 1998; Tan *et al.*, 2001; Jackson *et al.*, 2002]. Dihedral angles, where two curved GBs meet, are always small, around  $10^{\circ}$ . No parallel-sided melt layers at the submicron scale have been identified. As for the melt-free aggregates described previously [Jackson *et al.*, 2002] dislocation densities are very low, with the majority of the grains free of dislocations. Grain growth (Table 1) during hot pressing and thermal cycling prior to the final mechanical testing [see Jackson *et al.*, 2004] eliminated dislocations from the San Carlos olivine starting material.

[21] In many locations, image contrast in the olivine adjacent to GBs oscillated distinctly at a scale of tens of nanometers along the GB, an unexplained effect presumed due to local stress concentrations [see also Hiraga *et al.*, 2002, Figure 5]. In the coarser grained AT6366, grain boundaries were cracked open in some cases and faces separated by about 10 nm.

#### 3.2. Imaging and Analysis

[22] For GBs aligned parallel to the TEM beam, the minimum image width is normally close to 1 nm. A reversed double fringe effect accompanies change from underfocus to overfocus, indicating a narrow region which does not have olivine structure. However, despite intensive effort, direct high magnification imaging of GBs carefully aligned parallel to the viewing beam did not prove the existence of a continuous GB film. Images like Figure 6 suggest however that a narrow, disordered region between adjacent olivine grains is characteristic of olivine-olivine grain boundaries.

[23] The chemistry of the GB region was investigated by TEM using the elongate ‘broad’ beam method [Drury and Fitz Gerald, 1996]. Briefly, a beam of about  $25 \times 250$  nm in size is held on the GB for ca. 300 live seconds while an EDS X-ray analysis is made. The beam is then moved 50–100 nm away from the GB for a similar analysis in the margin of one of the adjacent olivine crystals. Very small peaks of Ca, Al, and Ti are almost always present in spectra from the volume centered on the GB, but are always absent from the spectra from the adjacent grains. The peak to background (P/B) ratio of the trace elements is well below

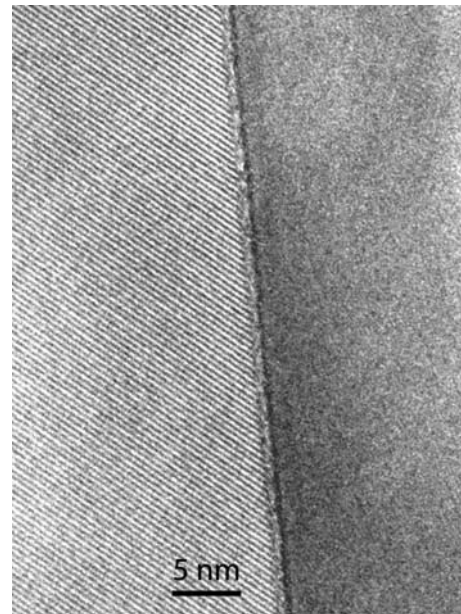


**Figure 6.** A high-magnification TEM image from a grain boundary in the slice of AT6384 re-equilibrated at  $1300^{\circ}\text{C}$  for 6h. Great care was taken to align this GB precisely parallel to the electron beam. Strong lattice fringes are imaged in the left side grain. The right side grain was not oriented to produce any fringe patterns. Note the region ca. 1 nm across at the center of the GB that shows different contrast from that of either grain. Images like this, or similar micrographs with no lattice fringes, were routinely recorded from many of the GBs examined in all the samples in this study.

that needed for quantitative analysis, so results are shown on P/B plots such as Figure 7. Non-GB analyses from olivine margins define fields that are distinctly different from those of GB analyses. The interpretation is that the non-GB fields indicate the sensitivity limit of the method, and that the GB region is enriched in Ca, Al and Ti. It is notable in Figure 7 that the GB enhancement in AT6384 is distinctly higher than in AT6366, which is consistent with the difference in olivine minor and trace element content detected by Microprobe WDS analysis (Table 4) and the difference in melt composition.

#### 3.3. Nanolenses

[24] Most grain boundaries in coarse-grained specimens AT6384 and AT6366 contain nanolenses of amorphous silicate (Figure 8). While difficult to prove, lenses lying on inclined boundaries suggest circular shapes in the plane of the lens. Nanolenses average around 200 nm in diameter and 20 nm in maximum thickness. While up to 25% of GB length is occupied by lenses in some places and other GBs are lens-free, on average, lenses are estimated to occupy around 5% of the total GB area. Very few lenses contain any crystalline phases. Presumably the nanolenses formed very early in the aggregate synthesis when small melt volumes were trapped on mobile GBs of the rapidly coarsening aggregates. Similar features, up to 2  $\mu\text{m}$  in diameter, were described from GBs in the very coarse-grained specimen AT6328 [Tan *et al.*, 2001], prepared from San Carlos olivine

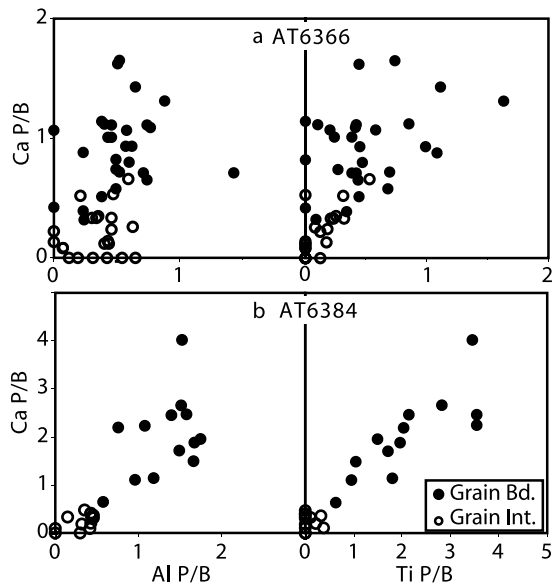


**Figure 7.** TEM-EDS analyses at and near grain boundaries in (a) AT6366 and (b) AT6384. Peak/background (P/B) ratios from X-ray spectra are plotted for Ca, Ti and Al signals. Analyses from GB regions (filled symbols) are distinctly different from those in nearby grains (open symbols). There is clear enrichment of Ca, Ti and Al in the GB regions. The elongate electron beam method was used, see text for details.

without added melt, but containing <0.01 vol% glass. No dissipation peak was resolved for this sample.

[25] TEM EDS analysis of the lenses (using the elongate electron beam) produces strong signals for not only Al, Ca and Ti, but also Na, K and Si, as for bulk glass analyses. The higher P/B ratio arising from the largest examples of these features allows statistically significant chemical analyses from corrected peak intensities, although overlap with adjacent olivine and beam volatilization problems suggest caution in interpreting single analyses. Nevertheless, lenses analyzed in both AT6366 and AT6384 show clear trends. In AT6366, the composition of the lenses is very like the bulk glass composition in triple junctions, while in AT6384 lenses and bulk glass are significantly different. Based on a corrected analysis from the largest lens in AT6384, lens chemistry is reasonably like that of the added basaltic glass, while the composition of triple junction glass reflects modification by the extensive crystallization described above. For AT6366, the similarity of the lens and bulk glass compositions can be attributed to the crystallization of only opx, as a consequence of the different melt composition. The entrapment of nanolenses on grain boundaries maybe similar to the process of melt inclusion formation in natural rocks; both are sufficiently rare that they are of no consequence for the bulk physical properties investigated here.

### 3.4. Summary and Comparison With Other Studies on Grain Boundaries

[26] All olivine-olivine grain boundaries investigated (melt-free and melt-bearing, sol-gel and San Carlos origin) are characterized by a narrow region, about 1 nm wide or

less, lacking olivine structure (Figures 6 and 11a). In the grain boundaries of melt-free sol-gel olivine samples no Ca, Al or Ti is detected, in accordance with the purity of the bulk olivine. Melt-free San Carlos olivine boundaries contain Ca, Al and Ti [Tan *et al.*, 2001]. Where Ca, Al and Ti are added to the sol-gel samples with the basaltic glass, they are incorporated as minor and trace elements into previously pure olivine crystals (Table 3). The narrow GB region also incorporates these minor and trace elements corresponding to their availability (Figure 7). Consequently, the GB enrichment in Ca, Al and Ti (Figure 7) does not form by expulsion (segregation) of excess trace elements from olivine interiors, but is the result of the approach to equilibrium partitioning of these elements between bulk melt, grain boundaries and grain interiors.

[27] The minor and trace element enrichment at olivine-olivine grain boundaries relative to olivine grain interiors is now well established [Drury and Fitz Gerald, 1996; Tan *et al.*, 1997; Cmíral *et al.*, 1998; de Kloe *et al.*, 2000; Tan *et al.*, 2001; Hiraga *et al.*, 2002; 2003; Jackson *et al.*, 2002]. The interpretation of images of grain boundaries is more controversial i.e., whether a grain-boundary film can actually be resolved [e.g., de Kloe *et al.*, 2000, Hiraga *et al.*, 2003]. As indicated above, we argue, based on the observation from our images, that lattice planes of neighboring grains do not directly abut. Regardless of the interpretation of images, the atomic structure of grain boundaries has to be significantly modified from that of olivine grain interiors to accommodate the higher minor and trace element content. Since the minor and trace element enrichment is an equilibrium feature, it will be present in natural rocks, and hence their grain boundary properties will have the same characteristics as those of our samples.

### 4. Models for Strain Energy Dissipation at High Temperature and Low Frequency in Crystalline Solids

[28] The dissipation peak so consistently observed in the present study is clearly associated with the presence of melt.

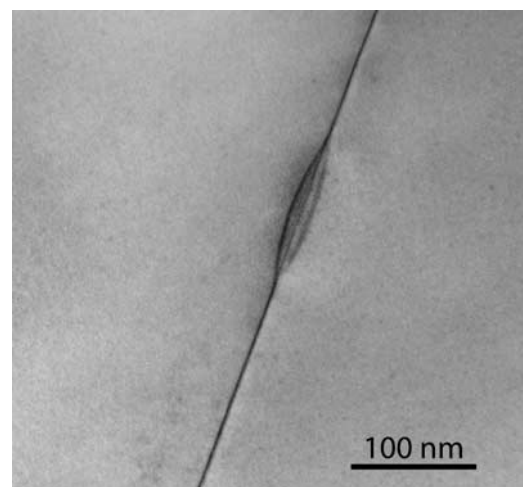


**Figure 8.** A nanolens of amorphous material on a GB of AT6384. Similar features, usually somewhat larger, are common in both AT6384 and AT6366.

However, this peak is superimposed on a dissipation background that is very similar to that for melt-free olivine aggregates. In an attempt to provide a coherent plausible explanation for the dissipation behavior of both melt-free and melt-bearing materials, available models and their assumptions are examined first (section 4) before their predictions are compared with experimental observations (section 5).

#### 4.1. Relaxation Mechanisms Responsible for Dissipation Peaks

[29] In a fluid-saturated rock, solid and fluid respond differently to the imposition of nonhydrostatic stresses from shear waves or torsional forced oscillation. It is typically assumed that the response of fluid-saturated rocks involves elastic deformation of the solid matrix, mediated by stress relaxation and flow of the fluid. *Jackson et al.* [2004] introduced the following four distinct fluid stress regimes: glued, saturated-isolated, saturated-isobaric and drained [*O'Connell and Budiansky*, 1977]. The drained regime involves exchange of fluid with an external reservoir; this sample-scale fluid flow is too slow to be relevant in our case [*Renner et al.*, 2003]. The transitions between glued and saturated-isolated, and saturated-isolated and saturated-isobaric regimes are potentially relevant to the interpretation of our results since each is associated with a dissipation peak.

[30] The transition from the glued regime, where the rock behaves as if there were no fluid present (i.e., purely elastic), to the saturated-isolated regime, where shear stresses in the fluid are relaxed but no grain-scale fluid flow takes place (“viscous shear,” [*Walsh*, 1968, 1969]) occurs at the shortest timescales. This is identical to the process of elastically accommodated grain-boundary sliding, discussed extensively in the materials science literature [e.g., *Raj and Ashby*, 1971], where each grain boundary is modeled as if it were a narrow crack containing a fluid of relatively low viscosity. This mechanism is further discussed in sections 4.2.1 and 4.3. At longer timescales the transition from saturated-isolated to saturated-isobaric involves grain-scale pressure-driven fluid flow (melt squirt, *Mavko and Nur* [1975]). The characteristic timescale for each of the two transitions depends on the viscosity of the fluid (or grain boundary material) as well as the aspect ratio (the ratio of width to length) of the fluid-filled inclusions (or grain boundary regions). These timescales are discussed in Section 4.3.

#### 4.2. The Raj-Ashby Model of Grain Boundary Sliding

[31] The following is a brief review of the classic model for grain-boundary sliding, developed by *Raj and Ashby* [1971], *Mosher and Raj* [1974] and *Raj* [1975]. It is widely invoked in discussions of high-temperature mechanical behavior [e.g., *Pezzotti et al.*, 1996; *Gribb and Cooper*, 1998; *Jackson et al.*, 2002]. The Raj-Ashby analysis provides an attractively comprehensive model for the viscoelastic behavior of fine-grained materials under conditions of low stress and high temperature that can be critically compared with experimental observations.

##### 4.2.1. Grain Boundary Sliding With Elastic Accommodation

[32] *Raj and Ashby* [1971] modeled elastically accommodated sliding between hexagonal grains in two dimensions.

They envisaged that a relative tangential displacement of neighboring grains due to an externally applied stress is facilitated by relaxation of boundary parallel shear stresses within a narrow region of relatively low viscosity. The necessary compatibility of grain shapes across the slipped boundary is maintained by purely elastic distortion of the adjacent grains resulting from a modified distribution of normal stress along the boundary. Following the removal of the external applied stress, this distribution of normal stress causes reversal of the grain-boundary sliding, meaning that the process of elastically accommodated grain-boundary sliding is anelastic. It was further assumed that no diffusion occurs during elastically accommodated sliding.

[33] The grain-boundary viscosity  $\eta_b$  is critical in determining the rate of such elastically accommodated grain-boundary sliding, and hence the unique anelastic relaxation time  $\tau_e$

$$\tau_e = \frac{M\eta_b}{G_U\alpha_b}. \quad (1)$$

In equation (1)  $G_U$  is the unrelaxed shear modulus,  $\alpha_b = \delta/d$  is the aspect ratio of the grain-boundary region of thickness  $\delta$  for grain size  $d$ , and  $M$  is a numerical factor of order 1 [*Kê*, 1947; *Nowick and Berry*, 1972; *Mosher and Raj*, 1974; *O'Connell and Budiansky*, 1977; *Ghahremani*, 1980]. The creep function for the *Raj and Ashby* [1971] model for elastically accommodated grain-boundary sliding, describing the response to unit step function shear stress application at  $t = 0$ , is thus that for the standard anelastic solid, i.e.,

$$J_e = J_U \left( 1 + \Delta \left( 1 - e^{-t/\tau_e} \right) \right), \quad (2)$$

where  $\Delta$  is the relaxation strength. Laplace transformation of this creep function yields the variation with frequency or period of the shear modulus between the unrelaxed shear modulus  $G_U = J_U^{-1}$  and the relaxed shear modulus  $G_R = G_U / (1 + \Delta)$ . The frequency-dependent strain energy dissipation  $Q^{-1}$  takes the form of a Debye peak of height  $(\Delta/2)(1 + \Delta)^{-1/2}$  [*Nowick and Berry*, 1972].

##### 4.2.2. Grain Boundary Sliding With Diffusional Accommodation

[34] The distribution of normal stress that prevails following completion of elastically accommodated grain boundary sliding defines the initial condition for transient diffusional creep or diffusionally accommodated grain boundary sliding as modelled by *Raj* [1975]. During the transient phase the distribution of grain boundary normal stress evolves from this initial state to that required by grain shape compatibility during steady state diffusional creep [*Raj and Ashby*, 1971]. The transient diffusional creep is well approximated by the second term,  $\beta t^n$  [*Jackson et al.*, 2004, equation (1)] of the Andrade creep function (also *Gribb and Cooper* [1998]). As pointed out previously by *Jackson et al.* [2000], this creep function implicitly involves a monotonic and infinitely wide distribution of anelastic relaxation times and therefore does not result in a dissipation peak.

[35] The transient creep rate  $\dot{\epsilon}_t$ , calculated by *Raj* [1975] is enhanced relative to the corresponding steady state diffusional creep rate  $\dot{\epsilon}_{ss}$  by a numerical factor that is a

function only of  $t/\tau_d$ .  $\tau_d$  is a measure of the duration of the transient given by

$$\tau_d = \frac{(1-\nu)kTd^p}{40\pi^3 G_U \delta D_b \Omega}. \quad (3)$$

In equation (3)  $D_b$ ,  $\Omega$ ,  $\nu$  and  $k$  are respectively the grain-boundary diffusivity, molecular volume of the diffusing species, Poissons ratio and Boltzmann's constant. The exponent  $p$  of the grain size sensitivity of  $\tau_d$  assumes values of 2 and 3 respectively for lattice and boundary diffusion. Thus

$$\dot{\epsilon}_{tr} = f\left(\frac{t}{\tau_d}\right) \dot{\epsilon}_{ss} \approx C\left(\frac{t}{\tau_d}\right)^{-q} \frac{\sigma}{\eta_{ss}} \quad (4)$$

where  $\sigma$  is the shear stress,  $\eta_{ss}$  the steady state viscosity and  $C$  and  $q$  constants. The latter expression, with  $C = 0.63$  and  $q \sim 0.44$  provides a good approximation to the variation of  $\dot{\epsilon}_{tr}$  with  $t/\tau_d$  displayed in Figure 10 of *Raj* [1975].

[36] Accordingly the creep function for *Raj*'s [1975] model of diffusively accommodated grain-boundary sliding, inclusive of both the transient and steady state creep regimes, is

$$J_d(t) = \left( \frac{C\tau_d^q}{(1-q)\eta_{ss}} \right) t^{1-q} + \frac{t}{\eta_{ss}}. \quad (5)$$

The creep function for the transient diffusional creep thus has the Andrade form  $\beta t^n$  with

$$\beta = \frac{C\tau_d^q}{(1-q)\eta_{ss}} \quad (6)$$

and  $n = 1 - q$  as recognized and emphasized by *Gribb and Cooper* [1998].

[37] The shear modulus dispersion and associated dissipation predicted by this model are readily evaluated from the Laplace transform of  $J_d(t)$  - including critical aspects such as the implied sensitivity of  $Q^{-1}$  to the variation of period  $T_o$  and grain size  $d$ . Both  $\tau_d$  and  $\eta_{ss}$  vary as  $d^p$  giving  $\beta \sim d^{-pn}$ . The result is a wide anelastic absorption band within which  $Q^{-1} \sim T_o^n d^{-pn}$  [e.g., *Jackson et al.*, 2000]. With  $p = 2$  or 3 and  $n \sim 1/2$  [*Raj*, 1975; *Gribb and Cooper*, 1998], the model predicts  $Q^{-1} \sim T_o^{1/2} d^{-s}$ , with  $s = 1$  or  $3/2$ .

[38] By combining the creep functions (equations (2) and (5)) for the elastically and diffusively accommodated grain-boundary sliding one obtains finally the single creep function that provides a comprehensive description of the linear mechanical behavior for the *Raj-Ashby* model solid. (Strictly speaking the need for prior elastically accommodated sliding requires a suitably delayed origin time for diffusively accommodated sliding.)

#### 4.3. Anelastic Relaxation Timescales

[39] From the foregoing discussion candidate mechanisms for the dissipation peak are melt squirt between triple junction tubules, melt squirt between ellipsoidal inclusions and elastically accommodated grain boundary sliding. The

relaxation time for melt squirt between triple junction tubules was calculated by *Mavko* [1980] as:

$$\tau_{s,t} = \frac{160\eta_m}{K_m\alpha_t^2} \quad (7)$$

where  $\alpha_t = 2R/d$  is the aspect ratio of the tubules (diameter/length),  $K_m$  is the bulk modulus of the melt and  $\eta_m$  the viscosity of the melt. The relaxation time for melt squirt between ellipsoidal inclusions is given by *O'Connell and Budiansky* [1977] as

$$\tau_{s,e} = \frac{2\pi\eta_m}{K_S\alpha_e^3} \quad (8)$$

where  $K_S$  the bulk modulus of the solid and  $\alpha_e$  the aspect ratio (width/length) of the inclusions. The relaxation time for elastically accommodated grain boundary sliding is given by equation (1) above with  $M = 2\pi$  [*O'Connell and Budiansky*, 1977].

[40] Contours of relaxation time as a function of aspect ratio and viscosity for the three mechanisms are shown in Figure 9. Each contour is the locus of all combinations of aspect ratio and viscosity that yield a particular relaxation time. With reference to an arbitrary point  $(\alpha_1, \eta_1)$  on a contour for relaxation time  $\tau_1$ , higher aspect ratios ( $\alpha > \alpha_1$  or more nearly equant melt pockets) or lower viscosities ( $\eta < \eta_1$ ), or both, are associated with a shorter relaxation time  $\tau < \tau_1$ . Mechanical testing at a period  $T_o \geq \tau_1$  would then sample conditions that are relaxed with respect to this particular relaxation mechanism. Conversely, points that plot above the  $\tau_1$  contour, i.e., at lower aspect ratios or higher viscosities or both, result in unrelaxed conditions for period  $T_o \leq \tau_1$ . For a given mechanism to produce a relaxation peak centered within our experimental period range (1–1000 s) it is therefore required that the relaxation time calculated as a function of aspect ratio and viscosity fall between the 1 s and 1000 s contours indicated in Figure 9.

[41] Figure 10 illustrates the sequence and combined impact of the various relaxation mechanisms in a plot of shear modulus (10a) and dissipation (10b) vs. period. At short periods ( $\sim 10^{-5}$  s) melt squirt between tubules (Figure 9a) is expected for melt with bulk viscosity. Melt squirt involving ellipsoidal inclusions of aspect ratios between 0.01 and 0.1 occurs at somewhat longer periods (but still  $\ll 1$  s). Elastically accommodated grain boundary sliding should result in dissipation at periods of about 1 s for grain boundary viscosities of the order of  $10^5$  Pa s (Figure 9c). The associated relaxation strength is an order of magnitude larger than for melt squirt between tubules (see sections 5.1.2 and 5.2 below). At periods much longer than those in our experiments we would expect squirt between the thin grain-boundary regions of material having grain boundary viscosity. The dissipation peaks and modulus dispersion associated with these anelastic relaxation mechanisms are superimposed in Figure 10 upon a monotonically period- and temperature-dependent background, arising from diffusively accommodated grain boundary sliding further discussed below.

#### 5. Comparison of Experimental Results With Models

[42] The very low dislocation densities essentially eliminate dislocation related mechanisms [e.g., *Karato and*

*Spetzler, 1990*] as explanation for the observed dissipation and modulus reduction. The conditions of low stress [*Jackson et al., 2004*], high temperature and small grain size (Table 1) are conducive for diffusional creep as the steady state deformation mechanism [e.g., *Hirth and Kohlstedt, 1995; Gribb and Cooper, 1998*]. The linear behavior observed in the low-strain tests of the present study therefore plausibly involves the processes described in section 4 as mechanisms for the experimentally observed viscoelastic relaxation.

### 5.1. The Case Against Melt Squirt

[43] Two dissipation mechanisms can potentially produce the dissipation peak observed in the present study: melt squirt and elastically accommodated grain boundary sliding. Because no peak is observed for our melt-free aggregates [*Jackson et al., 2004; Jackson et al., 2002*] it is tempting to attribute the dissipation peak to melt squirt. However, two separate lines of arguments suggest that this is unlikely:

#### 5.1.1. Melt Viscosity, Aspect Ratios and Crystallization

[44] From section 2 it is evident that there are two different temperature regimes (above and below 1200°C) which need to be examined separately. At 1200°C and above, the melt composition is basaltic with viscosities between 1 and 100 Pa s [*Murase and McBirney, 1973*]. The relaxation times given in sections 4.2.1 and 4.3 depend on aspect ratio and viscosity; for a particular relaxation mechanism to be relevant it is required that the peak position (period) correspond to the relaxation times calcu-

lated for the range of plausible viscosities and aspect ratios for our experiments (Figure 9).

[45] The cross-sectional diameter of the triple junction tubules in specimen 6366 with a melt content <0.4% and the largest grain size ranges from ~200 nm to a couple of  $\mu\text{m}$ . AT6380 with a mean grain size of 6.5  $\mu\text{m}$  has triple junction diameters of about 40 nm. These specimens therefore have the smallest triple-junction aspect ratios of the 6 specimens, ranging from about  $3 \times 10^{-3}$  to perhaps  $10^{-1}$ . Specimens 6335 and 6410 with average grain sizes around 10  $\mu\text{m}$  and average triple junction sizes of around 1  $\mu\text{m}$  have triple junction aspect ratios around  $10^{-1}$ . The triple junction size for the other two samples is most commonly between 1 and 5  $\mu\text{m}$ , resulting in aspect ratios greater than  $10^{-2}$ .

[46] The experimentally observed peak position is at periods shorter than 1 s at temperatures of 1200°C and above [*Jackson et al., 2004, Figures 13 and 14*]; the smallest triple junction tubule aspect ratios observed in our samples could therefore produce a peak in these specimens (6366 and 6380, Figure 9a). However, for triple junction tubule aspect ratios around  $10^{-1}$ , typical of specimens 6335 and 6410, the melt viscosity would have to be unrealistically high ( $10^4$  Pa s) for melt squirt to produce a relaxation peak at 0.01 s and 1300°C.

[47] The minimum aspect ratios for ellipsoidal melt inclusions are of the order of  $10^{-2}$  (Section 2.2, Figure 3). As for melt squirt between triple junction tubules, the relaxation times are smaller than the experimental oscilla-

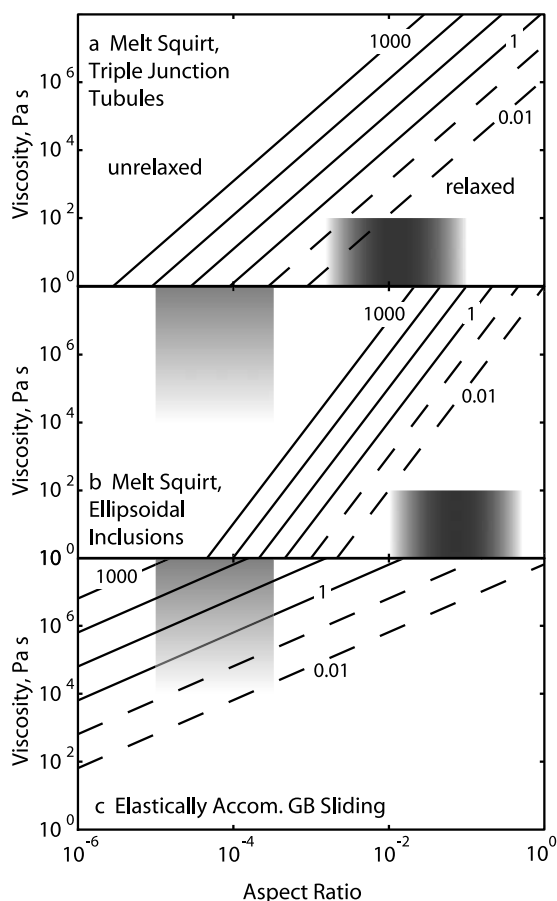


**Figure 9.** Relaxation times in viscosity-aspect ratio space for elastically accommodated grain-boundary sliding and melt squirt (*Schmeling [1985]*). Solid lines in the diagrams are lines of constant relaxation time (peak position in viscosity – aspect ratio space) and cover the period range used in our experiments; the numbers indicate period in seconds. Conditions above each line are unrelaxed for the indicated period, below the line relaxed with respect to the mechanism indicated in the diagram (see text). The dashed lines indicate relaxation times where the peak is outside our experimental period range (at temperatures of 1200°C and above [see *Jackson et al. [2004]*]). (a) Melt squirt between triple junction tubules. The contours for constant relaxation times are calculated from equation (7) with a melt bulk modulus of 20 GPa. The gray shading indicates the range of melt viscosity as it applies from 1300°C to 1200°C in our experiments, prior to extensive crystallization of cpx and plagioclase at lower temperatures, and the tubule aspect ratios determined for our samples. (b) Melt squirt between ellipsoidal inclusions. The contours for constant relaxation time are calculated from equation (8) with a bulk modulus of the solid of 100 GPa. Horizontal shading indicates the range of aspect ratios for inclusions >100 nm wide for which bulk melt viscosity applies. Vertical shading indicates the range of aspect ratios of  $\leq 1$  nm wide grain-boundary regions with viscosities ( $\eta_{gb}$ ) 100 to  $10^6$  times bulk melt viscosity (see text). (c) Elastically accommodated grain-boundary sliding. The contours for constant relaxation time are calculated from equation (1). The range of aspect ratios and possible grain boundary viscosities (gray shading) for relaxation by elastically accommodated grain boundary sliding falls into the period range used in our experiments.

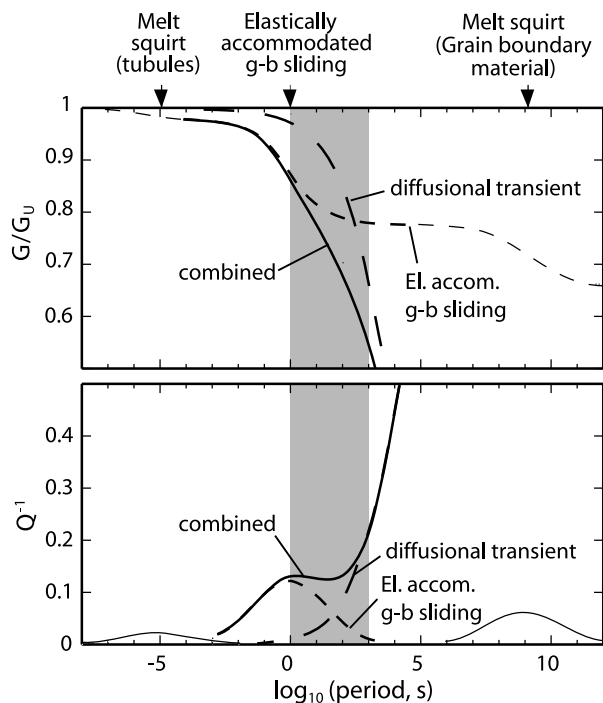


**Figure 10.** A semi-quantitative illustration of modulus relaxation and dissipation expected from relaxation mechanisms associated with grain-boundary sliding and melt squirt (for  $T = 1200^\circ\text{C}$ ,  $G_U = 60$  GPa,  $\alpha_t = 0.03$  and  $\alpha_{gb} = 3 \times 10^{-5}$ ). The relaxation times  $\tau_{s,t}$ ,  $\tau_e$  and  $\tau_{gb}$  are  $10^{-5}$  s, 1 s and  $10^9$  s respectively for melt squirt in tubules, elastically accommodated grain boundary sliding and melt squirt of the grain boundary material.

tion periods and peak positions at the highest temperatures (Figure 9b). *Hammond and Humphreys* [2000] similarly concluded from finite element modeling of melt geometries taken from *Faul et al.* [1994] that melt squirt occurs at relaxation times  $< 1$  s.

[48] Between  $1200^\circ\text{C}$  and  $1150^\circ\text{C}$  most of the melt crystallizes; but the dissipation peak at  $1000^\circ\text{C}$  is unchanged in height and shape relative to that observed at  $1200^\circ\text{C}$  [*Jackson et al.*, 2004] with the samples (except for 6366) now 99.95% crystalline (Figure 5). It would seem unlikely that the nanocrystalline plagioclase, that fills the former melt pockets and is attached to large olivine grains bounding the former melt pockets, squirts between triple junctions of different orientation at  $1000^\circ\text{C}$  in the same way the melt did at  $1200^\circ\text{C}$  and above. Conversely the melt in sample 6366 does not crystallize nanocrystalline plagioclase (i.e., is a glass at room temperature), but as for the other samples, the peak remains essentially unchanged over the temperature range from  $1000$  to  $1240^\circ\text{C}$ . It is therefore very unlikely that melt squirt produces the relatively uniform dissipation peak for all samples from  $1000^\circ\text{C}$  to  $1300^\circ\text{C}$ .

### 5.1.2. Relaxation Strength and Peak Height

[49] The relaxation strength  $\Delta$  for melt squirt between tubules has been calculated by *Mavko* [1980] and is modest ( $\Delta_t = 0.02$ ) even for the highest melt content in our aggregates ( $\phi = 3.7\%$ ). A  $Q^{-1}$  Debye peak height  $B$  no greater than  $\sim 0.01$  would therefore be expected, and the associated small modulus reduction would be difficult to

detect in our experiments. These predictions for melt squirt are clearly inconsistent with the substantial peak height (up to 0.13) and associated modulus dispersion that we observe [*Jackson et al.*, 2004].

### 5.2. The Case for Elastically Accommodated Grain Boundary Sliding

[50] Identifying the observed peak with the process of elastically accommodated grain boundary sliding explains a number of aspects of the behavior of the attenuation peaks listed by *Jackson et al.* [2004]. A primary constraint is the experimentally observed peak height and associated relaxation strength. Relaxation strengths calculated by *Zener* [1941] and *Kê* [1947] as well as by *Raj and Ashby* [1971] and *Ghahremani* [1980] for elastically accommodated grain boundary sliding are much larger than that predicted for melt squirt at the same melt content (see above and relative peak heights in Figure 10). The predictions for elastically accommodated grain boundary sliding are consistent with our experimental observations, whereas the predictions for melt squirt underestimate the experimentally observed peak heights considerably.

[51] *Jackson et al.* [2004, Figure 11] noted the influence of grain size on the location in period-temperature space of the peak for different specimens. In our Gaussian pseudo-period model [*Jackson et al.*, 2004, equation (21)] the peak period  $T_{op}$  varies as  $T_{op} \sim d \exp(E_p/RT)$  with  $m = 1$ , i.e., the location of the peak varies linearly with grain size. *Raj and Ashby's* [1971] equation for elastically accommodated grain boundary sliding (equation (1)) shows the same linear dependence of the relaxation time on grain size. In detail, the predicted difference in relaxation time at a fixed temperature between the most fine-grained and the most coarse-grained specimen ( $\sim$  a factor of eight in grain size) corresponds well to the observed difference in peak location of approximately one log unit in period [*Jackson et al.*, 2004, Figure 11]. In contrast, the relaxation times for melt squirt between tubules and ellipsoidal inclusions vary with grain size raised to the second and third power, respectively (equations (7) and (8), Figure 9).

[52] Even though images of grain boundaries in our olivine aggregates are suggestive only of a  $\leq 1$  nm disordered region between grains, it is reasonable to infer that the minor and trace element enrichment, enhanced grain boundary diffusivities relative to olivine grain interiors [*Farver and Yund*, 2000] and the macroscopic creep behavior of similar materials [*Hirth and Kohlstedt*, 1995] all indicate that the grain boundaries are weaker than the grain interiors. With the peak location in temperature-period space [*Jackson et al.*, 2004, equation (21) and Table 4] identified with the relaxation time  $\tau_e$  for elastically accommodated grain boundary sliding (equation (1)) we estimate grain boundary viscosities of  $10^4$  Pa s at  $1300^\circ\text{C}$  to  $10^9$  Pa s at  $1000^\circ\text{C}$  for a representative aspect ratio of  $10^{-4}$  (grain size  $10 \mu\text{m}$  with  $1$  nm wide boundary region). These viscosities are, reasonably, significantly larger than bulk melt viscosities but still much smaller than the viscosities of  $10^{12}$ – $10^{14}$  Pa s determined for our melt-bearing specimens from the microcreep tests of *Jackson et al.* [2004, Table 2, Figure 9]. The strong temperature dependence of the inferred grain boundary viscosity results from the high activation energy  $E_p$  for the dissipation peak.

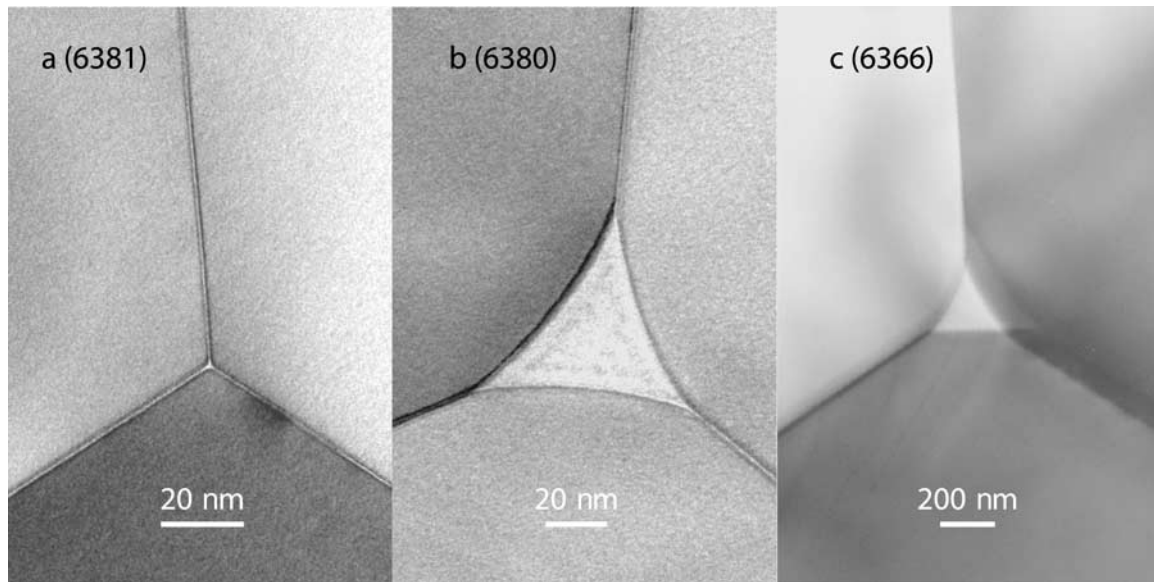


**Figure 11.** TEM images of three-grain edge intersections in (a) a melt-free sample [Jackson *et al.*, 2002] and (b, c) melt-bearing samples. (a) The triple junction area is only about 2 nm in diameter in the melt-free sample AT6381. (b) Typical triple junction in AT6380 with an estimated melt content of 0.01%. Examination of 40 three-grain edge intersections show that 39 are occupied by silicate glass with a relatively uniform diameter of about 40 nm. No larger, more irregular melt geometries have been found. (c) Triple junction tubule filled with melt (now glass) in AT6366. Forty three-grain edge intersections were investigated by TEM, all contained a silicate glass. There is a large range in triple junction tubule size in this sample (see Figure 1d).

[53] The fitted peak width ( $\sigma$ ) for the individual specimens given by Jackson *et al.* [2004, Table 1] shows that AT6384 has the narrowest ( $\sigma = 2.4$ ) and AT6335 and AT6380 the broadest peaks ( $\sigma = 3.2$ – $3.3$ ). Correspondingly AT6384 has the narrowest and AT6335 and AT6380 the broadest normalized grain size distributions (Figure 4 and Jackson *et al.* [2002]). This relationship between peak width and grain size distribution is consistent with the notion that the experimentally observed peak is broadened relative to the Debye peak for a unique grain size due to a distribution of timescales (equation (1)) corresponding to the range of grain sizes in the specimens.

[54] Finally, as described in more detail below, the variation of dissipation peak height with melt fraction for this suite of specimens is plausibly related to the variation in radius of curvature at olivine grain-edge triple junctions.

### 5.3. Grain Boundary Sliding in Melt-Free Aggregates

#### 5.3.1. Variation in Grain Boundary Viscosity

[55] Despite intensive sampling of the transition from elastic through dominantly anelastic into largely viscous behavior we do not see for genuinely melt-free olivine polycrystals any indication of a dissipation peak of significant height ( $B > 0.01$ ) that could plausibly be attributed to elastically accommodated grain-boundary sliding [Jackson *et al.*, 2002; Jackson *et al.*, 2004]. In principle, it is possible that the relaxation time  $\tau_e$  (equation (1)) for the melt-free materials at 1000–1300°C could be less than the periods typical of mechanical spectroscopy measurements ( $10^{-1}$ – $10^3$  s), meaning that the dissipation peak predicted for elastically accommodated grain-boundary sliding may have been overlooked. In this scenario, the variation of  $\tau_e$  with

temperature through the grain boundary viscosity  $\eta_b$  (equation (1)) is such that the peak would occur for the same oscillation periods at a lower temperature. Given our intensive sampling of frequency-temperature space, there is simply no possibility that a peak of height  $\sim 0.1$  could have been overlooked (e.g., Tan *et al.* [2001], Figure 9).

[56] Systematically lower grain-boundary viscosities in melt-bearing materials provide a potentially more viable explanation. With grain-boundary viscosities too high for elastically accommodated grain-boundary sliding in the melt-free materials under the accessible experimental conditions, the observed absorption-band behavior could be attributed to diffusively accommodated grain-boundary sliding. However, the presence/absence of a dissipation peak and its height are not clearly correlated with grain boundary chemistry. Melt-free sol-gel olivine samples show no resolvable peak, almost no Ca or other trace elements in the grain interiors and no detectable Ca in the grain boundaries. San Carlos olivine samples to which no melt has been added contain Ca and other trace elements in both the grain interiors and grain-boundaries, but their peak height correlates with melt content rather than grain boundary chemistry. High magnification TEM images of grain boundaries away from triple junctions for melt-free and melt-bearing samples are indistinguishable; all show the  $\leq 1$  nm wide region lacking olivine structure.

#### 5.3.2. Rounding of Grain Edges

[57] A consistent microstructural difference between melt-free and melt-bearing aggregates with potential implications for the mechanical behavior is shown in Figure 11. Figure 11a shows a TEM image of a typical triple junction in the melt-free sol-gel material, Figure 11b an image of a

triple junction in AT6380 with 0.01% melt and Figure 11c one of the smallest triple-junction tubules from AT6366 with 0.4% melt. The melt-free triple junction diameter is about 2 nm, whereas in the presence of melt the triple junction diameter is 10 to 100 times larger at the lowest melt contents for which a dissipation peak can be resolved.

[58] Comparing models for spheres [Zener, 1941; Ké, 1947] (relaxation strength  $\Delta \sim 0.8$ ) with those for more realistic geometries (hexagonal grain shapes, [Raj and Ashby, 1971], and finite element modeling of hexagonal grains ( $\Delta \sim 0.23$ ) [Ghahremani, 1980]) suggests that rounding of corners increases the sliding distance and hence enhances the relaxation strength. Decreasing sharpness of grain edges at triple junctions causing increasing relaxation strength would also explain the increasing peak height with increasing melt content [Jackson *et al.*, 2004, Figure 10]. It has also been previously suggested that (sharp) grain edges might impede grain-boundary sliding [Raj and Ashby, 1971; Ghahremani, 1980]. We tentatively conclude therefore that the rounding of grain edges in the melt-bearing aggregates relative to the melt-free aggregates facilitates elastically accommodated grain boundary sliding in the former and explains the observed dissipation peak.

#### 5.4. Shortcomings of the Raj-Ashby Model of Grain Boundary Sliding

[59] Raj and Ashby [1971] represent grain boundary topography, the distribution of stresses and the associated strains by Fourier series. However the sum in the denominator of their equation (2) (p. 1115) does not converge, so that their predictions for a hexagonal geometry dependent on truncation of the infinite series are mathematically problematical. The calculations are correct however for an assumed sine-wave grain boundary geometry.

[60] The Raj – Ashby model of deformation associated with grain boundary sliding envisages an initial stage of elastically accommodated sliding, followed by the diffusional transient, and finally steady state diffusional creep. However, unless the grain boundary viscosity is zero, elastically accommodated sliding must occur at a finite rate and thus require a finite time  $\tau_e$ . This means that sliding with elastic accommodation and sliding facilitated by diffusion must actually overlap in time, inconsistent with the initial conditions for the distribution of stress assumed by Raj [1975] for the diffusional transient. Our experimental observations clearly show that the attenuation peak associated with elastically accommodated sliding in the melt-bearing materials is superimposed on an exponentially increasing background attributed to diffusionally accommodated sliding, confirming that the two processes occur concurrently.

[61] The sliding distance for elastically accommodated grain boundary sliding (equation (6) and Raj and Ashby [1971, p. 1116]) predicted for the typical conditions of our experiments (shear stress  $\sim 0.2$  MPa [Jackson *et al.*, 2004],  $G_U \sim 60$  GPa and  $d \sim 10$   $\mu\text{m}$ ) is at most  $\sim 0.01$  nm, i.e., significantly smaller than interatomic bond lengths. Under these circumstances a continuum description of the mechanical behavior of the grain boundary region must become questionable.

[62] Moreover, the measured period and grain size dependences of  $Q^{-1} \sim (T_0 d)^{1/4}$  in melt-free olivine aggregates

are much milder than predicted for diffusionally accommodated grain boundary sliding. This mild frequency and grain size dependence, close to the elastic threshold [Jackson *et al.*, 2002, Figure 9], was the basis for our original inference that elastically accommodated grain boundary sliding might be the dominant mechanism for the observed dissipation. Instead, it now seems possible that elastically accommodated sliding is suppressed altogether in melt-free materials.

[63] If elastically accommodated sliding is effectively suppressed for melt-free aggregates, the initial conditions for the Raj [1975] analysis of transient diffusionally accommodated grain boundary sliding would be inappropriate. The appropriate initial conditions for the consideration of diffusion would be the distribution of normal stress acting perpendicular to the boundary in the elastically deformed state, with both normal and shear stresses, acting across the boundary, taken into account in assessing mechanical equilibrium. The future development of such a model might provide an explanation for the relatively mild frequency and grain-size sensitivity of  $Q^{-1}$  near the threshold for elastic behavior, and predict more accurately the relaxation strength as a function of grain boundary geometry.

[64] We therefore infer, like Gribb and Cooper [1998], that the monotonically increasing background dissipation in both melt-free and melt-bearing samples is due to diffusionally accommodated grain boundary sliding. However, for the reasons given earlier in this section, the absence of a resolvable peak for the melt-free samples is inconsistent with Gribb and Cooper's assumption that the grain boundary shear viscosity is negligible, and their associated suggestion that the peak might occur at very short periods [Gribb and Cooper, 1998, p. 27,274]. Also, it follows from the foregoing discussion that the Raj [1975] model with its assumption of prior elastically accommodated sliding cannot be expected to provide a quantitatively reliable description of the diffusional transient.

#### 5.5. Activation Energy

[65] For melt-bearing olivine aggregates the background activation energy  $E_B$  is 520 kJ/mol, whereas the peak activation energy is 720 kJ/mol (261 data,  $T = 1000$ – $1300^\circ\text{C}$ , [Jackson *et al.*, 2004, Table 4]. Melt-free  $E_B$  is 400 kJ/mol (90 data,  $T = 1000$ – $1300^\circ\text{C}$ , [Jackson *et al.*, 2004, Table 4]. From grain boundary diffusion creep experiments Hirth and Kohlstedt [1995] determined an activation energy for “nominally” melt-free aggregates (no added melt but containing an estimated 0.5–1 vol. % impurity derived melt, Hirth and Kohlstedt [1995, p. 1985]) of 315 kJ/mol ( $T = 1200$ – $1250^\circ\text{C}$ , and an activation energy of 575 kJ/mol for aggregates with more than 4–5% melt present ( $T = 1110$ – $1300^\circ\text{C}$ ). Kohlstedt and Zimmerman [1996], referring to work by Zimmerman *et al.* [1992] give for a spinel lherzolite at 0.3 GPa a subsolidus activation energy for diffusional creep of 340 kJ/mol ( $T = 1000$ – $1160^\circ\text{C}$ ), and a supersolidus activation energy of 610 kJ/mol ( $T = 1160$ – $1300^\circ\text{C}$ ). Few details on sample composition, melt distribution, temperature dependence of melt content or determination of the solidus are available for these experiments.

[66] The bulk composition of the melt-bearing aggregates in our study is very similar to the bulk composition of Hirth and Kohlstedt [1995]; therefore if the higher activation

energy in their 4–5% melt content samples is due to the temperature dependence of the melt content as they infer, similar considerations will also apply to our results. Alternatively, the enhanced background activation energy of the melt-bearing relative to melt-free samples could be related to melt-enhanced diffusion. As indicated above (section 5.2) attribution of the peak to elastically accommodated grain-boundary sliding associates the corresponding activation energy  $E_p$  with the viscosity of the grain boundary region.

## 6. Comparison With Other Studies

### 6.1. Partially Molten Olivine Aggregates

[67] The data from the present study are most closely comparable with those of *Gribb and Cooper* [2000] for a specimen of reconstituted dunite of 2.8  $\mu\text{m}$  average grain size containing 5 wt% added potassic melt. The dissipation measured by Gribb and Cooper is 30–100% higher at 1200–1250°C than for our most fine-grained basaltic-melt-bearing specimen AT6335 ( $d = 8.9 \mu\text{m}$ ,  $\phi = 2.1\%$ ). That this difference is only partly attributable to the difference in grain size and melt content is demonstrated by the extent to which our global model underestimates the attenuation observed by Gribb and Cooper (Figure 12a). Moreover, the Gribb and Cooper data contain no evidence of the melt-related dissipation peak so consistently seen for our melt-bearing olivine materials. Indeed, the qualitatively similar monotonic absorption-band behavior for the nominally melt-free reconstituted dunite of *Gribb and Cooper* [1998] and their melt-added material was strongly emphasized [*Gribb and Cooper*, 2000].

[68] However, the sampling of a wide period-temperature domain was critical for our consistent observation of the broad melt-related dissipation peak in the present study. With experimental observations confined to a much narrower domain of temperature and/or oscillation period the peak could easily have been missed. For example, the dissipation data for specimen 6335 confined to 1150–1250°C and 1–100 s would not strongly suggest the presence of a peak [*Jackson et al.*, 2004, Figure 2]. *Gribb and Cooper* [2000] report the testing of their very fine-grained melt-added specimen over the temperature range 900–1285°C at periods of 3–200 s, but the only data actually presented are for the narrow temperature interval 1200–1285°C. For their grain size of 2.8  $\mu\text{m}$  and melt content of 5%, our global model for basaltic melt-bearing olivine [*Jackson et al.*, 2004, Table 4,  $N = 261$  fit] predicts a peak of height  $B = 0.18$  centered at  $T_o = 0.08$  s at 1200°C - well outside Gribb and Cooper's observational range. Lower temperatures of  $\sim 1030$ – $1120^\circ\text{C}$  are required to bring the predicted peak center into the 3–200 s period range.

[69] The dissipation reported by *Kampfmann and Berckhemer* [1985] for Åheim dunite of 300  $\mu\text{m}$  average grain size and for a synthetic forsterite polycrystal of 1 mm average grain size compare reasonably well with the background component of our global model (Figures 12b and 12c). The frequency dependence of the measured dissipation becomes systematically milder than for the model background for periods  $< 1$  s for both the dunite and synthetic forsterite - suggestive of the presence of a broad dissipation peak located at shorter periods than prescribed by our model. Indeed a dissipation peak

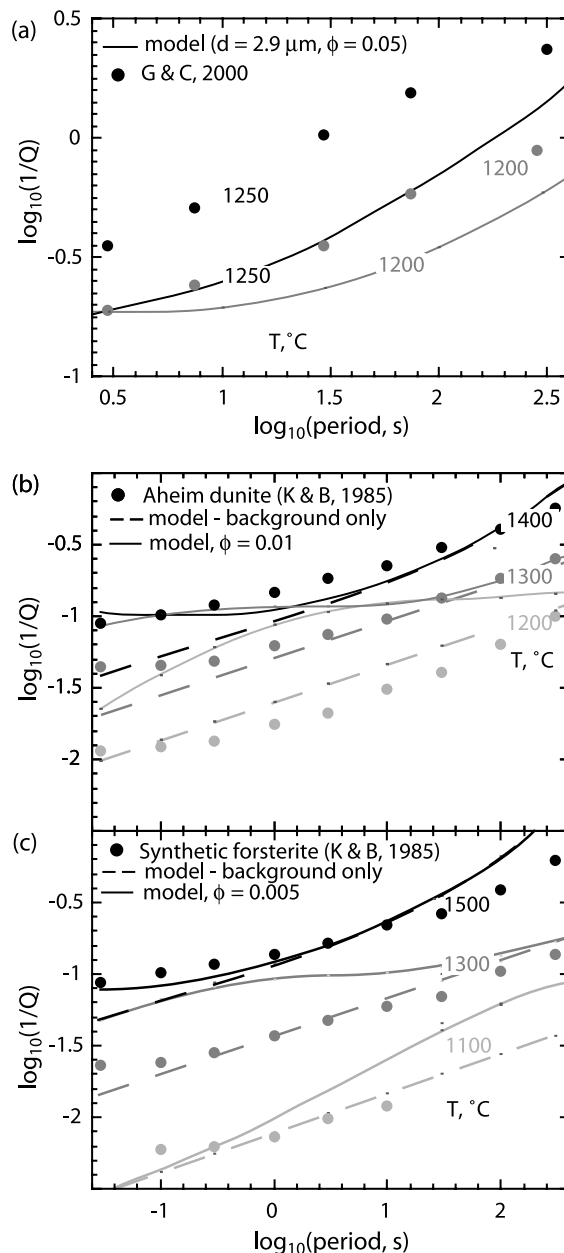


**Figure 12.** (a) Comparison of the  $Q^{-1}$  data (filled circles) of *Gribb and Cooper* [2000] from torsional forced oscillation test on a reconstituted dunite of 2.8  $\mu\text{m}$  average grain size, containing 5 wt% added potassic melt, with the prediction for the same grain size and melt fraction from the global model [*Jackson et al.*, 2004, Table 4,  $N = 261$ ] of the present study (curves). (b) Comparison of representative torsional forced oscillation data (plotting symbols) of *Kampfmann and Berckhemer* [1985] for Åheim dunite of 300  $\mu\text{m}$  average grain size with the global model from this study [*Jackson et al.*, 2004, Table 4,  $N = 261$ ] continuous curves) evaluated at the same grain size and an indicative melt content of 1%. The dashed lines indicate the background component of the global model for the melt-bearing polycrystalline olivine. (c) as for (b) but for the synthetic forsterite polycrystal ( $d = 1$  mm) of *Kampfmann and Berckhemer*, assumed for the purpose of modeling to have an impurity-derived melt content of 0.5%. See color version of this figure in the HTML.

identified by Kampfmann and Berckhemer in data for a peridotite pseudotachylite (and various other igneous rocks) bears a striking resemblance to that seen in the present study. Their dissipation peak was generally adequately modelled with a Gaussian distribution of relaxation times with a standard deviation of about 3 [Jackson *et al.*, 2004, Tables 1 and 4] and the peak moved systematically to shorter period with increasing temperature with a relatively high activation energy of  $\sim 400$ – $600$  kJ/mol [Kampfmann and Berckhemer, 1985].

[70] A dissipation peak, at first glance strikingly similar to our observations, has been reported in a parallel study of fine-grained basaltic melt-bearing olivine polycrystals [Xu *et al.*, 2003]. Using a torsional pendulum technique confined to essentially constant resonant periods in the range 0.1–0.5 s, these authors identified a pronounced  $Q^{-1}(T)$  dissipation peak centered near  $1200^{\circ}\text{C}$ , superimposed upon an exponentially temperature dependent background for each of several specimens with melt contents ranging from 0.4–13%. The peak position (e.g.,  $1200^{\circ}\text{C}$  at 0.5 s period and  $20\ \mu\text{m}$  grain size [Xu *et al.*, 2003, Figure 10.2]) is in excellent agreement with that predicted [Jackson *et al.*, 2004, equation (21)] from the global model fitted to the data of the present study [Jackson *et al.*, 2004, Table 4,  $N = 261$ ].

[71] However, there are also some striking differences. The dissipation peaks observed by Xu *et al.* [2003] are adequately represented by the Debye peak of the standard anelastic solid [Jackson *et al.*, 2004] and are thus much narrower than those of our study. The peak height observed by Xu *et al.* [2003] varies linearly with melt fraction from  $B = 0.13$  for  $\phi = 0.4\%$  to  $B = 0.32$  at  $\phi = 13\%$  (their Figure 10.5). That this  $B(\phi)$  trend extrapolates to a finite value of peak height at zero melt fraction is used by Xu *et al.* to argue that the same mechanism (elastically accommodated grain-boundary sliding) should also be operative in melt-free materials. The height of our much broader dissipation peak is lower and requires representation by a  $B(\phi)$  power law with  $B = 0$  at  $\phi = 0$  [Jackson *et al.*, 2004, Figure 10]. The activation energies of 310 (50) and 330 (50) kJ/mol describing the variation of peak position (period) with temperature for the samples with  $\phi = 0.4\%$  and  $\phi = 6\%$ , respectively, are much lower than those (615 (50) and 650 (50) kJ/mol, respectively) describing the temperature-dependent background [Xu *et al.*, 2003]. For our specimens, the situation is reversed with higher activation energy for peak position than for background (for example, for the  $N = 261$  global model,  $E_P = 720$  kJ/mol and  $E_B = 520$  kJ/mol).

[72] These differences might be attributable to the contrasting testing protocols employed in the two studies. The specimens of Xu *et al.* [2003] were tested at essentially fixed (resonant) period during relatively rapid temperature cycling. In contrast, the results of our study were obtained from a wide variation of oscillation period under isothermal conditions at each of a series of temperatures during slow staged cooling. The reported absence of crystallization of the basaltic melt during the course of the Xu *et al.* [2003] tests, in contrast with the results of the present study, implies thermodynamic disequilibrium. Without published microstructures, grain size distributions or chemical analyses by Xu *et al.* [2003] it is difficult to compare the two studies. Also, the measurements by Xu *et al.* [2003] and Gribb and Cooper [2000] were performed at atmospheric

pressure, unlike those of the present study performed on jacketed specimens under 200 MPa confining pressure.

[73] In summary, our global model for the frequency, temperature, grain-size and melt-fraction sensitivity of  $Q^{-1}$  correctly predicts the location of the dissipation peak seen by Xu *et al.* [2003] and can explain the absence of a peak at  $1200$ – $1285^{\circ}\text{C}$  in the study by Gribb and Cooper [2000]. In general, however, the lack of detailed information concerning grain-boundary structure and chemistry and melt distribution and composition in these studies, and the known complication of thermal microcracking in the Kampfmann and Berckhemer [1985] study of relatively coarse-grained specimens preclude further quantitative interpretation.

## 6.2. Nonoxide Si-Based Ceramics

[74] Dissipation peaks attributed to grain-boundary processes have also been observed for nonoxide ceramics [e.g., Mosher *et al.*, 1976; Pezzotti *et al.*, 1996].  $\text{Si}_3\text{N}_4$  and SiC in particular exhibit a number of similarities, both in melt distribution and mechanical behavior, with polycrystalline olivine. The Si based non-oxide ceramics almost always contain a silicic glass phase due to exposure of the precursor powders to atmospheric oxygen. As for our melt-bearing olivines, the siliceous melt occupies tubules at all three-grain edges and some larger pockets. In addition, all grain boundaries in these materials contain a continuous film about 1 nm thick [e.g., Clarke, 1987, Pezzotti *et al.*, 1996].

[75] The key features of the mechanical behavior are the following: Firstly, the dissipation peak for  $\text{Si}_3\text{N}_4$  and SiC with their pure oxynitride or oxycarbide melts moves to shorter period with increasing temperature but is otherwise unchanged in height and width [Pezzotti *et al.*, 1996]. A peak width that is independent of peak-top temperature implies a unique activation energy and hence chemical uniformity of the grain boundary material [Niblett, 1961]. Relative to the Debye peak of the standard anelastic solid, the observed peak is much broader (about two decades wide), requiring a distribution of relaxation times attributed to geometrical variability (i.e., a distribution of grain sizes and grain boundary angles [Nowick and Berry, 1972, Pezzotti, 2001]). This behavior of the peak mirrors that in partially molten olivine in our study.

[76] Secondly, without a melt phase present, the monotonically increasing background dissipation is observed without a superimposed peak again as for melt-free olivine [Pezzotti *et al.*, 1997, 1998]. Microstructurally, the  $\text{SiO}_2$ -free silicon carbides and nitrides show the same abutting three-grain edge intersections as melt-free olivine (compare Figure 3 in Pezzotti *et al.* [1997] with our Figure 11a). Thirdly, the activation energy for the peak is much higher than the activation energy for the background [Pezzotti *et al.*, 1996].

[77] It is interesting to note that Pezzotti *et al.* [1996, 1998, 2000] find only a small relaxation strength ( $\Delta \sim 0.02 - 0.03$ ) for their melt-bearing  $\text{Si}_3\text{N}_4$  and SiC materials. They argue that the attenuation peak in their experiments is due to elastically accommodated grain boundary sliding, but that the numerical factor in the equation for the sliding distance by Raj and Ashby [1971, equation (6), p. 1116] is too high and is better constrained by their experimental observations. However, the  $\text{SiO}_2$  melt phase in the  $\text{Si}_3\text{N}_4$

and SiC aggregates has a much higher viscosity ( $>10^6$  Pa s, [Pezzotti *et al.*, 2000]) than the basaltic melt in our samples. With a viscosity of order  $10^6$  Pa s and aspect ratios that are broadly similar to those in our melt-bearing samples the frequencies of their experiments (3.3–12.7 Hz) fall in the range where melt squirt between grain-edge tubules and ellipsoidal inclusions should be active as a relaxation mechanism (Figures 9a and 9b). This would be consistent with their small measured relaxation strength and could also explain why the peak activation energies determined by Pezzotti *et al.* [1996, 2000] are similar to those for SiO<sub>2</sub> bulk melt viscosity. In contrast, the peak activation energies for the melt-bearing olivine aggregates are much higher than those for bulk basaltic melt, consistent with the notion that the material in the thin grain boundary regions does not have bulk melt properties.

## 7. Extrapolation of Global Fit to Mantle Grain Size and P-T Regime

### 7.1. Background

[78] Application of our high-temperature, seismic-period laboratory data to seismic wave attenuation in the upper mantle involves an extrapolation mainly in grain size and pressure. The extrapolation in grain size, facilitated by our measured grain-size dependence over one order of magnitude in grain size, is justified by the near steady state normalized grain-size distribution in most of our samples, – expected to be similar to the grain size distribution in the mantle outside of high-strain zones.

[79] The steady state grain-size distribution and the equilibration of the sol-gel olivine with the basaltic melt, indicated by the uptake of Ca, also indicates that chemical as well as textural equilibrium (or steady state) is reached, so that the melt distribution is expected to be similar to that in the mantle in the absence of high stress deformation. According to numerical models of mantle flow at mid-ocean ridges, stresses and strains in the upwelling part of the mantle are insignificant in comparison to those in the corner region where the flow turns horizontal [e.g., Ribe, 1989]. As the melt is produced in the upwelling portion, the present experiments are directly applicable. A similar argument applies for three-dimensional upwelling beneath slow spreading ridges where the strain in the central part of the upwelling, where most of the melt is produced, is also small [e.g., Choblet and Parmentier, 2001].

[80] As indicated above, we also expect a grain boundary structure and chemistry in mantle rocks that is similar to our experimental materials. The same dissipation mechanisms should therefore operate in the mantle as in our experiments. The only difference to natural rocks is the presence of the nanocrystalline plagioclase with residual glass at subsolidus temperatures in our materials. In natural rocks grain corners will be formed by abutting crystalline grains at subsolidus temperatures; a dissipation peak will therefore only be observable when melt is actually present above the solidus.

[81] For the extrapolation in pressure we have incorporated into each of equations (19) and (20) of Jackson *et al.* [2004] the factor  $\exp(-PV/RT)$ . In the absence of any more directly relevant information concerning the influence of pressure we have used the activation volume  $V$  ( $6 \times$

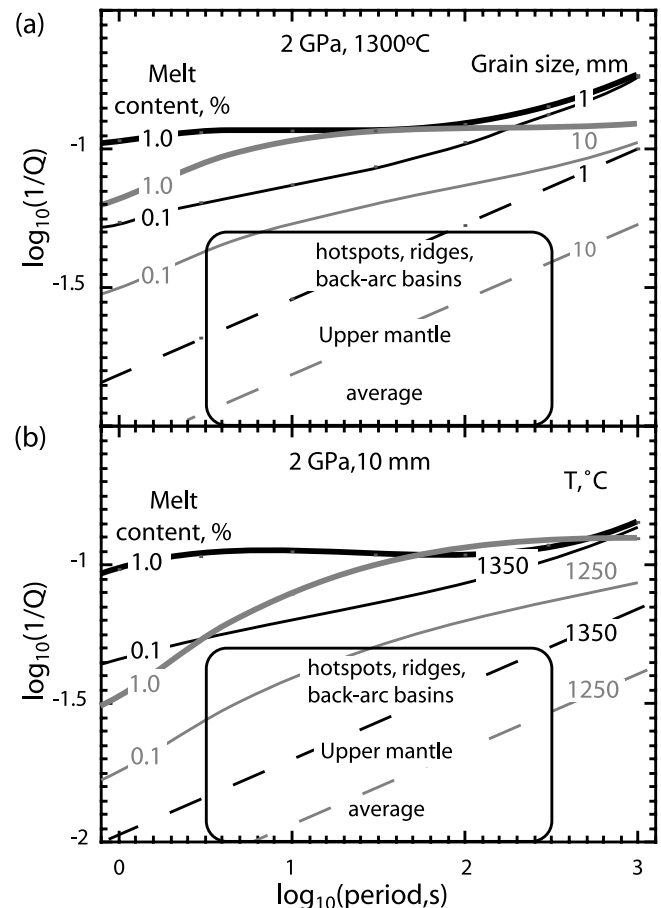


**Figure 13.** The global fit [Jackson *et al.*, 2004, Table 4,  $N = 261$ ] to the experimental observations of dissipation in melt-bearing olivine aggregates extrapolated to the larger grain sizes and P-T for decompression melting of upwelling mantle material. (a) Variation of  $Q^{-1}$  with grain size and melt fraction at 1300°C and 2 GPa. The lines with the same color all represent the same grain size, the thinning represents decreasing melt content. Dashed lines indicate the attenuation for the same grain size in the absence of melt. (b) Variation of  $Q^{-1}$  with temperature and melt fraction at 10 mm grain size and 2 GPa pressure. Color indicates temperature with line width again related to melt content. Dashed lines as for (a) represent melt-free behavior. See color version of this figure in the HTML.

$10^{-6}$  m<sup>3</sup>/mol) recently estimated for climb-controlled dislocation creep in olivine [Bejina *et al.*, 1999].

### 7.2. Extrapolation

[82] The global fit [Jackson *et al.*, 2004, Table 4,  $N = 261$ ] to the experimental observations of the frequency, temperature, grain-size and melt-fraction sensitivity of the dissipation in our fine-grained melt-bearing materials is thus readily and appropriately extrapolated to upper-mantle conditions. The results obtained for representative grain sizes of 1 and 10 mm, melt contents of 0.1 and 1%, and P-T conditions approximating those of partial melting in upwelling mantle material beneath mid-ocean ridges (2 GPa and 1300°C) are shown in Figure 13a. Unlike the situation for the fine-grained materials tested in the laboratory, the

melt-related dissipation peak is expected to be clearly evident at 1300°C and seismic frequencies for the 1–10 mm grain sizes. Consideration of Jackson *et al.* [2004, equation [21]] indicates that for  $m = 1$  the center of the dissipation peak is displaced by an amount

$$\delta \log_{10} T_o|_T = \delta \log_{10} d. \quad (9)$$

For  $d = 10$  mm, the peak position is such that superposition of the background and the long-period side of the dissipation peak leads to nearly frequency-independent attenuation. For the smaller grain size of 1 mm, the peak center is displaced to shorter periods by 1 order of magnitude, resulting in a lesser impact upon the frequency dependence of  $Q^{-1}$  in the seismic frequency band.

[83] The temperature dependence of the calculated attenuation at fixed grain size (10 mm) is shown in Figure 13b. As with the experimental data for the fine-grained materials, the temperature dependence of the calculated seismic wave attenuation is complicated by the displacement of the dissipation peak. Under appropriate conditions (e.g., a melt fraction of 1%) the temperature-induced displacement of the dissipation peak can combine with the temperature dependence of the background to produce minimal temperature dependence of  $Q^{-1}$  for much of the seismic frequency band. The levels of attenuation predicted by this extrapolation of laboratory data are generally somewhat higher than those ( $\sim 0.05$ ) determined seismologically in the more lossy parts of the upper mantle beneath hot spots and mid-ocean ridges and in mantle wedges above subduction zones (Figure 13). At face value, this would suggest very low average melt fractions ( $\sim 0.1\%$ ) and/or relatively large grain sizes ( $\geq 10$  mm). However, the spatial resolution of  $Q^{-1}$  studies is still relatively low ( $>200$  km horizontally [e.g., Selby and Woodhouse, 2002; Forsyth, 1992]) in comparison to regional P wave tomographic studies ( $\sim 50$  km [e.g., Dueker *et al.*, 2001]), such that averages through relatively large regions for  $Q^{-1}$  models may include both partially molten and melt-free upper mantle.

## 8. Conclusions

[84] The high-temperature viscoelastic behavior of fine-grained polycrystalline olivine aggregates is profoundly modified by the presence of a small melt fraction. A broad melt-related dissipation peak is superimposed upon a monotonically frequency and temperature dependent background enhanced relative to that for melt-free materials.

[85] For melt-bearing olivine, the dissipation is attributed to grain-boundary sliding with a combination of elastic and diffusional accommodation acting in parallel. We argue that the presence of triple-junction tubules  $>40$  nm in diameter facilitates elastically accommodated sliding to a sufficient degree to produce a broad dissipation peak - requiring a distribution of anelastic relaxation times two decades wide. This interpretation requires an effective viscosity for olivine-olivine grain boundary regions, observed to be  $\leq 1$  nm in width, that is much higher than for bulk basaltic melt but still substantially lower than for the olivine grain interiors, and also very strongly temperature dependent. The approximately linear variation of peak position (period) with grain size is consistent with this interpretation. The absence of

such a dissipation peak for genuinely melt-free olivine polycrystals of comparable grain size suggests that elastically accommodated grain-boundary sliding with a finite sliding distance is inhibited by the abutting grain-edge intersections. Comparison with other experimental studies of melt-bearing olivine aggregates shows that the global fit to our data correctly predicts the presence or absence of a dissipation peak in these studies, but other aspects remain to be explained [Gribb and Cooper, 2000; Xu *et al.*, 2003].

[86] The dissipation background for both melt-bearing and melt-free olivine aggregates is attributed to diffusional accommodation grain-boundary sliding. However, under period-temperature-grain size conditions close to the threshold for elastic behavior, the experimentally determined dissipation is more mildly frequency and grain-size sensitive than is predicted from the model of Raj [1975] for transient diffusional creep with its assumption of prior elastically accommodated sliding. Progress toward a definitive micromechanical understanding of high-temperature grain-boundary sliding will require modeling in which this assumption is abandoned.

[87] Meanwhile, extrapolation of the experimental data for melt-bearing olivine aggregates to the mm-cm grain sizes and P-T conditions of the upper mantle yields levels of attenuation generally somewhat higher than the spatially averaged values inferred seismologically for the more lossy parts of the upper mantle. Under appropriate conditions, the superposition of the melt-related dissipation peak upon the mildly frequency dependent background results in nearly frequency-independent attenuation across the teleseismic frequency band.

[88] **Acknowledgments.** We thank Joshua Carr for maintenance of the high-pressure laboratory, Harri Kokkonen for assistance with specimen preparation and characterization, Frank Brink from the ANU's electron microscopy unit, and Kay Provins and Dagmar Kelly for assistance with the preparation of the manuscript. Both Parts 1 and 2 of this manuscript were substantially improved in response to reviews by Associate Editor S. Karato and two anonymous reviewers. We thank Mervyn Paterson for a careful reading of the manuscripts and the suggestion that we use the term 'pseudoperiod' for the variables  $X_B$  and  $X_P$ .

## References

- Bejina, F., O. Jaoul, and R. C. Liebermann (1999), Activation volume of Si diffusion in San Carlos olivine: Implications for upper mantle rheology, *J. Geophys. Res.*, *104*, 25,529–25,542.
- Choblet, G., and E. M. Parmentier (2001), Mantle upwelling and melting beneath slow spreading centers: Effects of variable rheology and melt productivity, *Earth Planet. Sci. Lett.*, *184*, 589–604.
- Clarke, D. R. (1987), On the equilibrium thickness of intergranular glass phases in ceramic materials, *J. Am. Ceram. Soc.*, *70*, 15–22.
- Cmiral, M., J. D. Fitz Gerald, U. H. Faul, and D. H. Green (1998), A close look at dihedral angles and melt geometry in olivine-basalt aggregates: A TEM study, *Contrib. Mineral. Petrol.*, *130*, 336–345.
- de Kloe, R., M. R. Drury, and H. L. M. van Roermund (2000), Evidence for stable grain boundary melt films in experimentally deformed olivine-orthopyroxene rocks, *Phys. Chem. Min.*, *27*, 480–494.
- Drury, M. R., and J. D. Fitz Gerald (1996), Grain boundary melt films in an experimentally deformed olivine-orthopyroxene rock: Implications for melt distribution in upper mantle rocks, *Geophys. Res. Lett.*, *23*, 701–704.
- Dueker, K., H. Yuan, and B. Zurek (2001), Thick-structured proterozoic lithosphere of the Rocky Mountain Region, *GSA Today*, *11*, 4–9.
- Farver, J. R., and R. A. Yund (2000), Silicon diffusion in forsterite aggregates: Implications for diffusion accommodated creep, *Geophys. Res. Lett.*, *27*, 2337–2340.
- Faul, U. H., D. R. Toomey, and H. S. Waff (1994), Intergranular basaltic melt is distributed in thin, elongated inclusions, *Geophys. Res. Lett.*, *21*, 29–32.
- Forsyth, D. W. (1992), Geophysical constraints on mantle flow and melt generation beneath mid-ocean ridges, in *Mantle Flow and Melt Genera-*

- tion, edited by J. Phipps Morgan, D. K. Blackman, and J. M. Sinton, pp. 1–65, AGU, Washington D. C.
- Ghahremani, F. (1980), Effect of grain boundary sliding on anelasticity of polycrystals, *Int. J. Sol. Struct.*, *16*, 825–845.
- Gribb, T. T., and R. F. Cooper (1998), Low-frequency shear attenuation in polycrystalline olivine: Grain boundary diffusion and the physical significance of the Andrade model for viscoelastic rheology, *J. Geophys. Res.*, *103*, 27,267–27,279.
- Gribb, T. T., and R. F. Cooper (2000), The effect of an equilibrated melt phase on the shear creep and attenuation behavior of polycrystalline olivine, *Geophys. Res. Lett.*, *27*, 2341–2344.
- Hammond, W. C., and E. D. Humphreys (2000), Upper mantle seismic wave attenuation: Effects of realistic partial melt distribution, *J. Geophys. Res.*, *105*, 10,987–10,999.
- Hiraga, T., I. M. Anderson, M. E. Zimmerman, S. Mei, and D. L. Kohlstedt (2002), Structure and chemistry of grain boundaries in deformed olivine + basalt and partially molten lherzolite aggregates: Evidence of melt-free grain boundaries, *Contrib. Mineral. Petrol.*, *144*, 163–175.
- Hiraga, T., I. M. Anderson, and D. L. Kohlstedt (2003), Chemistry of grain boundaries in mantle rocks, *Am. Mineral.*, *88*, 1015–1019.
- Hirth, G., and D. L. Kohlstedt (1995), Experimental constraints on the dynamics of the partially molten upper mantle: Deformation in the diffusion creep regime, *J. Geophys. Res.*, *100*, 1981–2001.
- Jackson, I., J. D. Fitz Gerald, and H. Kokkonen (2000), High-temperature viscoelastic relaxation in iron and its implication for the shear modulus and attenuation of the Earth's inner core, *J. Geophys. Res.*, *105*, 23,605–23,634.
- Jackson, I., J. D. Fitz Gerald, U. H. Faul, and B. H. Tan (2002), Grain-size-sensitive seismic wave attenuation in polycrystalline olivine, *J. Geophys. Res.*, *107*(B12), 2360, doi:10.1029/2001JB001225.
- Jackson, I., U. H. Faul, J. D. Fitz Gerald, and B. H. Tan (2004), Shear wave attenuation and dispersion in melt-bearing olivine polycrystals: 1. Specimen fabrication and mechanical testing, *J. Geophys. Res.*, *109*, doi:10.1029/2003JD002406, in press.
- Kampfmann, W., and H. Berckhemer (1985), High temperature experiments on the elastic and anelastic behavior of magmatic rocks, *Phys. Earth Planet. Inter.*, *40*, 223–247.
- Karato, S., and H. A. Spetzler (1990), Defect microdynamics in minerals and solid-state mechanisms of seismic wave attenuation and velocity dispersion in the mantle, *Rev. Geophys.*, *28*, 399–421.
- Kê, T. S. (1947), Experimental evidence of the viscous behavior of grain boundaries in metals, *Phys. Rev.*, *71*, 533–546.
- Kohlstedt, D. L., and M. E. Zimmerman (1996), Rheology of partially molten mantle rocks, *Annu. Rev. Earth Planet. Sci.*, *24*, 41–62.
- Mavko, G. M. (1980), Velocity and attenuation in partially molten rocks, *J. Geophys. Res.*, *85*, 5173–5189.
- Mavko, G. M., and A. Nur (1975), Melt squirt in the asthenosphere, *J. Geophys. Res.*, *80*, 1444–1448.
- Mosher, D. R., and R. Raj (1974), Use of the internal friction technique to measure rates of grain boundary sliding, *Acta Metall.*, *22*, 1469–1474.
- Mosher, D. R., R. Raj, and R. Kossowsky (1976), Measurement of the viscosity of the grain boundary phase in hot-pressed silicon nitride, *J. Mater. Sci.*, *11*, 49–53.
- Murase, T., and A. R. McBirney (1973), Properties of some common igneous rocks and their melts at high temperatures, *Geol. Soc. Am. Bull.*, *84*, 3563–3592.
- Niblett, D. H. (1961), Low-frequency measurements of the Bordoni internal friction peak in copper, *J. Appl. Phys.*, *32*, 895–899.
- Nowick, A. S., and B. S. Berry (1972), *Anelastic relaxation in crystalline solids*, 677 pp., Academic, San Diego, Calif.
- O'Connell, R. J., and B. Budiansky (1977), Viscoelastic properties of fluid-saturated cracked solids, *J. Geophys. Res.*, *82*, 5719–5735.
- Pezzotti, G. (2001), Low-frequency measurements on the grain-boundary internal friction peak in chlorine-doped silicon nitride, *J. Am. Ceram. Soc.*, *84*, 2366–2370.
- Pezzotti, G., K. Ota, and H.-J. Kleebe (1996), Grain-boundary relaxation in high-purity silicon nitride, *J. Am. Ceram. Soc.*, *79*, 2237–2246.
- Pezzotti, G., H.-J. Kleebe, K. Ota, and K. Yabuta (1997), Suppression of viscous grain-boundary sliding in a dilute SiAlON ceramic, *J. Am. Ceram. Soc.*, *80*, 2349–2354.
- Pezzotti, G., H.-J. Kleebe, and K. Ota (1998), Grain-boundary viscosity of polycrystalline silicon carbides, *J. Am. Ceram. Soc.*, *81*, 3293–3299.
- Pezzotti, G., T. Wakasugi, T. Nishida, R. Ota, H.-J. Kleebe, and K. Ota (2000), Chemistry and inherent viscosity of glasses segregated at grain boundaries of silicon nitride and silicon carbide ceramics, *J. Non Cryst. Solids*, *271*, 79–87.
- Raj, R. (1975), Transient behavior of diffusion-induced creep and creep rupture, *Metall. Trans. A*, *6*, 1499–1509.
- Raj, R., and M. F. Ashby (1971), On grain boundary sliding and diffusional creep, *Metall. Trans.*, *2*, 1113–1127.
- Renner, J., K. Viskupic, G. Hirth, and B. Evans (2003), Melt extraction from partially molten peridotites, *Geochem. Geophys. Geosyst.*, *4*(5), 8606, doi:10.1029/2002GC000369.
- Ribe, N. M. (1989), Seismic anisotropy and mantle flow, *J. Geophys. Res.*, *94*, 4213–4223.
- Schmeling, H. (1985), Numerical models on the influence of partial melt on elastic, anelastic and electrical properties of rocks. Part 1: Elasticity and anelasticity, *Phys. Earth Planet. Inter.*, *41*, 34–57.
- Selby, N. D., and J. H. Woodhouse (2002), The  $Q$  structure of the upper mantle: Constraints from Rayleigh wave amplitudes, *J. Geophys. Res.*, *107*(B5), 2097, doi:10.1029/2001JB000257.
- Tan, B. H., I. Jackson, and J. D. Fitz Gerald (1997), Shear wave dispersion and attenuation in fine-grained synthetic olivine aggregates: Preliminary results, *Geophys. Res. Lett.*, *24*, 1055–1058.
- Tan, B. H., I. Jackson, and J. D. Fitz Gerald (2001), High-temperature viscoelasticity of fine-grained polycrystalline olivine, *Phys. Chem. Miner.*, *28*, 641–664.
- Waff, H. S., and J. R. Bulau (1979), Equilibrium fluid distribution in an ultramafic partial melt under hydrostatic stress conditions, *J. Geophys. Res.*, *84*, 6109–6114.
- Walsh, J. B. (1968), Attenuation in partially melted material, *J. Geophys. Res.*, *73*, 2209–2216.
- Walsh, J. B. (1969), New analysis of attenuation in partially-melted rock, *J. Geophys. Res.*, *74*, 4333–4337.
- Wirth, R. (1996), Thin amorphous films (1–2 nm) at olivine grain boundaries in mantle xenoliths from San Carlos, Arizona, *Contrib. Mineral. Petrol.*, *124*, 44–54.
- Xu, Y., M. E. Zimmerman, and D. L. Kohlstedt (2003), Deformation behavior of partially molten mantle rocks, in *MARGINS Theoretical and Experimental Earth Science*, edited by G. Karner, Columbia Univ. Press, New York, in press.
- Zener, C. (1941), Theory of elasticity of polycrystals with viscous grain boundaries, *Phys. Rev.*, *60*, 906–908.
- Zimmerman, M. E., G. Hirth, and D. L. Kohlstedt (1992), Deformation of partially molten lherzolite, *Eos Trans. AGU*, *73*(43), Fall Meet. Suppl., 529.

U. Faul, J. D. Fitz Gerald, and I. Jackson, Research School of Earth Sciences, The Australian National University, Canberra ACT 0200, Australia. (uli.faul@anu.edu.au)